







RESEARCH ARTICLE | APRIL 01 2025

Methods for energy dispersive x-ray spectroscopy with photon-counting and deconvolution techniques

Alessandro Forte ; Thomas Gawne ; Oliver S. Humphries ; Thomas Campbell ; Yuanfeng Shi ; Sam M. Vinko 



J. Appl. Phys. 137, 134501 (2025)

<https://doi.org/10.1063/5.0251153>



View
Online



Export
Citation

Articles You May Be Interested In

Subspace-constrained deconvolution of auditory evoked potentials

J. Acoust. Soc. Am. (June 2022)

Deconvolution of time series in the laboratory

Am. J. Phys. (October 2016)

Deconvolution of decomposed conventional beamforming

J. Acoust. Soc. Am. (August 2020)

10 April 2025 16:02:44

Instruments for Advanced Science

- Knowledge
- Experience
- Expertise

[Click to view our product catalogue](#)

Contact Hiden Analytical for further details:
www.HidenAnalytical.com
info@hiden.co.uk

Gas Analysis

- dynamic measurement of reaction gas streams
- catalysis and thermal analysis
- molecular beam studies
- dissolved species probes
- fermentation, environmental and ecological studies

Surface Science

- UHV TPD
- SIMS
- end point detection in ion beam etch
- elemental imaging - surface mapping

Plasma Diagnostics

- plasma source characterization
- etch and deposition process reaction kinetic studies
- analysis of neutral and radical species

Vacuum Analysis

- partial pressure measurement and control of process gases
- reactive sputter process control
- vacuum diagnostics
- vacuum coating process monitoring







Methods for energy dispersive x-ray spectroscopy with photon-counting and deconvolution techniques

Cite as: J. Appl. Phys. **137**, 134501 (2025); doi: [10.1063/5.0251153](https://doi.org/10.1063/5.0251153)

Submitted: 29 November 2024 · Accepted: 10 March 2025 ·

Published Online: 1 April 2025



Alessandro Forte,^{1,a)}  Thomas Gawne,^{2,3}  Oliver S. Humphries,⁴  Thomas Campbell,¹  Yuanfeng Shi,¹ 
and Sam M. Vinko^{1,5,b)} 

AFFILIATIONS

¹Department of Physics, Clarendon Laboratory, University of Oxford, Parks Road, Oxford OX1 3PU, United Kingdom

²Center for Advanced Systems Understanding (CASUS), Görlitz D-02826, Germany

³Helmholtz-Zentrum Dresden-Rossendorf (HZDR), Dresden D-01328, Germany

⁴European XFEL, Holzkoppel 4, 22869 Schenefeld, Germany

⁵Central Laser Facility, STFC Rutherford Appleton Laboratory, Didcot OX11 0QX, United Kingdom

^{a)}Author to whom correspondence should be addressed: alessandro.forte@physics.ox.ac.uk

^{b)}sam.vinko@physics.ox.ac.uk

ABSTRACT

Spectroscopic techniques are essential for studying material properties, but the small cross sections of some methods may result in low signal-to-noise ratios (SNRs) in the collected spectra. In this article, we present methods, based on combining Bragg spectroscopy with photon counting and deconvolution algorithms, which increase the SNRs, making the spectra better suited to further analysis. We aim to provide a comprehensive guide for constructing spectra from camera images. The efficacy of these methods is validated on synthetic and experimental data, the latter coming from the field of high-energy density (HED) science, where x-ray spectroscopy is essential for the understanding of materials under extreme thermodynamic conditions.

© 2025 Author(s). All article content, except where otherwise noted, is licensed under a Creative Commons Attribution (CC BY) license (<https://creativecommons.org/licenses/by/4.0/>). <https://doi.org/10.1063/5.0251153>

I. INTRODUCTION

The birth of spectroscopy as a scientific discipline can be traced back to Joseph von Fraunhofer's work with diffraction gratings, which were the first instruments to systematically divide the spectral component of electromagnetic radiation, dispersing them into distinct regions of space.¹ Following this, the invention of the photographic plate in the mid-19th century enabled the first permanent recording of spectral lines, representing the earliest example of a light detector. The following discovery of the photoelectric effect, along with the development of quantum mechanics to support the underlying theory, led to the development of modern detectors, such as photomultiplier tubes (PMTs)² and later semiconductor-based detectors such as charge-coupled devices (CCDs) and finally hybrid detectors,³ which are the widely used nowadays and will be the detectors considered in this work. These

detectors consist of individual units, called pixels, arranged in ordered arrays. Each pixel is composed of two distinct components (hence the term “hybrid”): A semiconductor layer that captures photon energy and a readout electronics layer that amplify and quantify the signal produced by the photon capture.

X-ray spectroscopy is an essential tool in multiple areas of physics as it enables the experimental examination of numerous material properties, including chemical composition, electronic structure, and dynamic processes at the atomic and molecular levels.⁴ The deep penetration of x rays allows for the exploration of bulk material properties, while their short wavelengths enable the excitation of inner-shell electrons and detailed probing of material structure, expanding the range of spectroscopic techniques available. The recent developments in bright x-ray sources, primarily led by x-ray free electron lasers (XFEL)⁵ and laser-plasma-generated

10 April 2025 18:02:44

sources,^{6,7} have been particularly beneficial to the field of high-energy density (HED) physics and the study of matter under extreme conditions of temperature, pressure, and density. Such systems are typically highly transient, short-lived, and created in small volumes and, thus, require a dedicated set of experimental diagnostics and data analysis approaches for their study. Modern x-ray sources are ideally suited to such explorations because of their short pulse durations (typically ps–fs, but access to the attosecond regime is readily available⁸), tunable photon energies, narrow bandwidths (ranging from $\sim 1\%$ to 0.01% of photon energy⁹), and access to high x-ray intensities up to $10^{22} \text{ W cm}^{-2}$.¹⁰ Importantly, much progress has been made in exploiting the short pulse durations of x rays for time-resolved studies of dynamical processes by coupling these sources with other drivers such as high-power or high-energy optical lasers.^{11–13}

In this work, we will focus on methods developed to cater to the needs of HED science, an area of growing importance due to its relevance to astrophysical phenomena¹⁴ and practical applications such as inertial confinement fusion energy^{15–17} and materials development.^{18,19} The short-lived nature of experimental realizations of such systems requires *in situ* diagnostics—often spectroscopic—to evaluate the physical properties of interest such as structure factors,^{20,21} ionization potential depression,^{22,23} x-ray opacities,^{24–26} and collisional ionization rates.^{27,28} This information can be extracted from “self-scattering” experiments, where the x rays both create and probe the extreme conditions^{29,30} or in “pump–probe” configurations where the samples are prepared using alternative drivers, and then probed at some later time by the x rays.^{31,32}

X-ray spectroscopy is predominantly performed using dispersive elements such as crystals or gratings, coupled with a detector in various geometries. These elements disperse (or selectively transmit in scanning mode³³) the spectral components of the radiation emitted by the target, which are then collected by the detector. In Sec. II B, we will analyze separately two of the most common crystal-based configurations in HED science: The flat crystal and the von Hámos geometries. Additionally, we will focus on how to treat camera images characterized by low photon counts, except for small regions around transition lines—a common occurrence in x-ray spectroscopy. These low photon numbers typically arise from the low cross sections of the spectroscopic processes employed, short exposure times, and limited solid angle coverage. If the photon density is low everywhere on the camera and resolution requirements are not stringent, single-photon counting spectroscopy (SPCS),³⁴ a method suited to pixel detectors, becomes preferable to dispersive spectroscopy. In SPCS, photon energies are determined based on the signal generated by each photon hit, rather than their position on the detector. Although SPCS is widely used with modern detectors, it falls outside the scope of this discussion and will not be covered in this article.

The objective of this work is first to provide a step-by-step guide on how to construct a spectrum from the initial detector images, a resource that, to our knowledge, is not found in the existing literature as a single comprehensive document but rather scattered across various sources. In doing this, we will also present methods for enhancing the signal-to-noise ratio (SNR) and the resolution of a camera image, which are capable of simultaneously

treating regions with high and low photon density. Despite these features being common and completely general, we will showcase these techniques on experimental data coming from HED science.

II. METHODS

In this section, we outline the techniques used to construct the spectrum from the initial camera image. For completeness, we will begin with a brief overview of how a semiconductor pixel detector works, which will be beneficial for subsequent discussions. Next, we will detail the process of finding the energy map for two of the most common types of spectrometers. Finally, we will explain how to go from the analog-to-digital units (ADU) map to the distribution of photon hits by means of single photon counting algorithms and image deconvolution techniques. In the following, we will disregard the physical processes that produce the photons arriving at the spectrometer and focus only on the problem of constructing a spectrum from the initial matrix A_{ij} , whose elements represent the total signal on pixel (i, j) . Here, the pixels form a two-dimensional array labelled by $i = 1, \dots, N_y$ and $j = 1, \dots, N_x$, with N_y and N_x representing the number of pixels in the vertical and horizontal directions, respectively. As an example, Fig. 1 illustrates the construction, from the corresponding camera image, of the emission spectrum of warm-dense MgF_2 . These data, taken from Ref. 23, were obtained by irradiating MgF_2 with intense x rays approximately 300 eV above the atomic K-edge of Mg (~ 1303 eV). As described in Ref. 30, this radiation generates a population of Mg and F ions in various ionization states, with their relative abundances determined by the rates of atomic processes. The energy of photons emitted during electron photodecays depends on the ionization state of the ion involved, yielding a series of spectral lines. The resulting spectrum is divided into different regions based on the signal intensity, which corresponds to the local photon density on the camera. These data will be analyzed in Sec. III B using the image processing methods introduced in Secs. II A–II E.

The construction of the spectrum can be divided into three sequential steps:

1. **Computing the energy map of the camera.** This process involves determining the energy associated with each pixel, E_{ij} . As we will see, these energies represent averaged values for each pixel, accounting for effects such as source broadening and finite pixel size. These effects mix the energies of photons hitting a single pixel, ultimately reducing the maximum achievable spectral resolution. Section II B details the techniques for computing this energy map.
2. **Estimating the photon hits on the detector.** For a given camera image, A_{ij} , this step calculates the most likely distribution of photon hits on the detector, N_{ij}^{γ} , providing a good estimate for the number of photons hitting each pixel (i, j) . The methods for performing this operation will be discussed in Sec. II D.
3. **Constructing the spectrum.** This final step involves placing N_{ij}^{γ} in the appropriate energy bin according to the energy map E_{ij} , with corrections applied for the varying solid angles associated with each energy level.

The details of how the image is converted to a spectrum depends on the specific geometry of the spectrometer. While all the

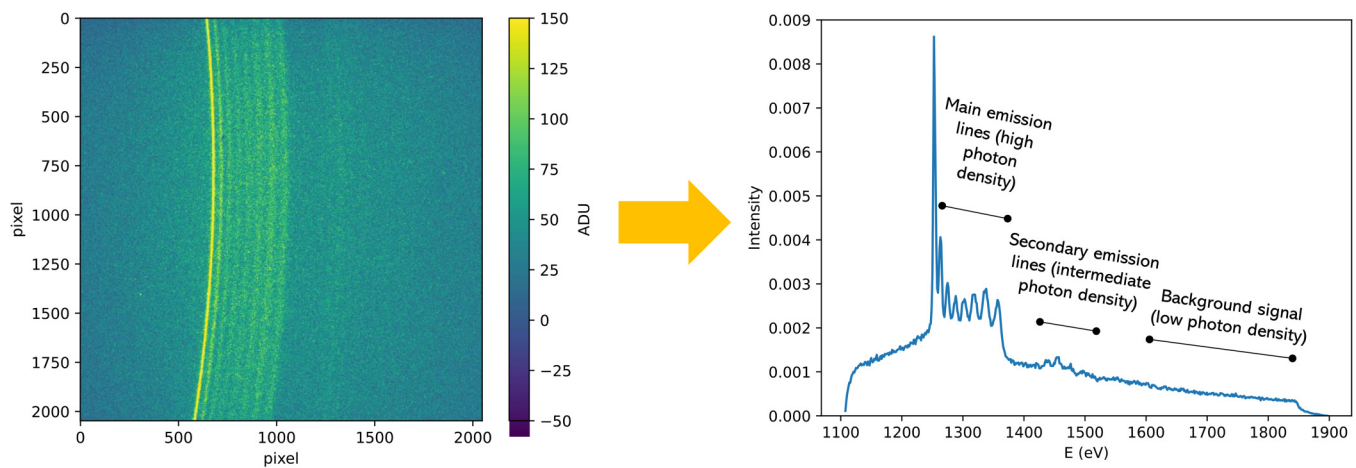


FIG. 1. Example of the construction of a spectrum (right) from the corresponding camera image A_{ij} (left), which is a 2048×2048 pixel array. The image presents areas with different photon densities, labelled in the associated spectrum. In this example, the signal is the emission spectrum of warm-dense MgF_2 from Ref. 23. The bright arcs in the image correspond to the $K\alpha$ and satellite emission lines, emitted from different ionization states of the Mg ions. The varying intensities of these lines reflect the relative abundance of ions in each state.

spectrometers relevant to this work are based on Bragg's law and this is ultimately used to construct the spectrum, in practice specific geometries (such as the von Hámós geometry, which is given some attention later) may allow for simpler dispersion equations.

A. Pixel detectors

Pixel detectors are integral components in the detection and measurement of light in various scientific applications, including spectroscopy, astronomy, and medical imaging. These detectors work by converting incoming photons into electronic signals that can be quantified and analyzed. A simplified diagram of a pixel detector is shown in Fig. 2. The general functioning of a pixel

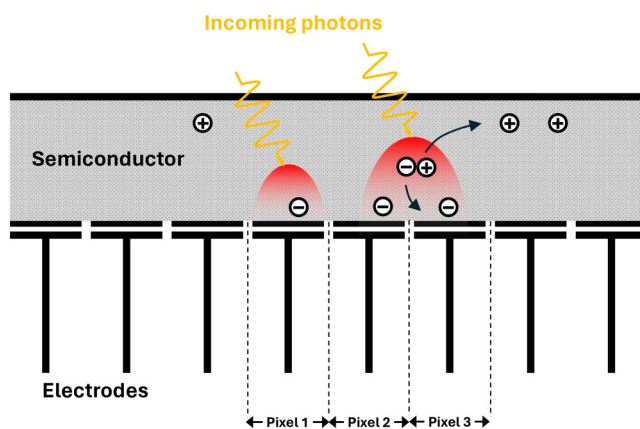


FIG. 2. Simplified scheme of a pixel detector section illustrating how charge spreading can distribute a photon across multiple pixels.

detector involves several stages: Photon absorption, charge generation and collection, charge transfer, and signal readout.

- 1. Photon absorption.** The process begins when photons enter the detector and strike the photosensitive surface, usually made of a doped or compound semiconductor (e.g., doped silicon, GaAs). At x-ray energies, photons interact with the semiconductor atoms via photoionization, generating electron-hole pairs. The number of these pairs is approximately proportional to the energy of the photon hitting the surface, with random fluctuations quantified by the Fano factor.³⁵ The efficiency in converting the photon energy into electrons energy is instead measured by the quantum efficiency (QE),³⁶ which is essentially the probability that a photon will be photoabsorbed, creating a photocurrent.
- 2. Charge Generation and Collection.** The generated electrons are collected in potential wells created by an array of electrodes on the detector surface. Each pixel in the detector corresponds to one potential well. The number of electrons collected in each well is roughly proportional to the energy contained in the light hitting that pixel, making the detector highly effective for capturing detailed images. However, thermal noise, which is intrinsic to the detector and depends on its temperature, can also generate electron-hole pairs, known as "dark current," which disturbs the measurement.³⁷ Additionally, the electron cloud generated by photon absorption can diffuse over multiple pixels, causing image blurring. This diffusion is quantified by the point spread function (PSF),³⁸ which is a two-dimensional decaying function (typically a Gaussian, but sometimes distorted) with a characteristic width referred to as charge spreading radius (R_s).^{39,40} The spreading radius can be estimated both theoretically and experimentally^{40,41} and depends on various parameters, including detector thickness and incoming photon energy. While reducing the sensor thickness can mitigate this spreading effect, it also

10 April 2025 18:02:44

decreases the probability of photon absorption, thereby impacting the quantum efficiency. Furthermore, even though R_s is rigorously dependent on the photon energy—affecting the depth at which the photon is absorbed (see Fig. 2)—we assume it to be constant in this article, as we can restrict our analysis to a portion of the detector illuminated by a sufficiently narrow photon energy range, thanks to Bragg spectroscopy.

3. **Charge Transfer.** Once the exposure is complete, the collected charge needs to be transferred to the readout electronics. For modern hybrid detectors, this is done *in situ* with the readout electronics connected to each individual pixel. In the case of CCDs, this is achieved through a process known as charge transfer, where the charges are moved sequentially through the CCD's structure to the output register. This transfer is carefully controlled to preserve the spatial information of the image. The loss of electrons occurring in this operation, which is not present in hybrid detectors, is measured by the so-called charge transfer efficiency.^{42,43} For these reasons, hybrid detectors offer faster and more accurate readout than traditional CCDs.
4. **Signal Readout.** In the final stage, the collected charges are read out by converting them into a voltage signal. This is done using a charge amplifier that translates the charge into a corresponding voltage. The voltage signal is then sent to an analog-to-digital converter (ADC), which converts it into digital counts known as analog-to-digital units (ADU).⁴⁴ These ADUs represent the total energy of the photons incident on each pixel, combined with noise, and form the basis of the digital image.

For our analysis, we are interested in knowing the following detector characteristics: R_s , the level of noise of each pixel, and the ADU counts associated to a photon of energy E , $ADU_{sp}(E)$, which will, in general, depend on the pixel. The noise on each pixel is measured simply by running the detector multiple times while the source is blocked (known as “dark runs”⁴⁵) and then looking at the statistics of the empty frames for each pixel across the different shots. The dark runs are taken regularly during an experiment to measure the pixel noise as the detector conditions naturally change over time, and their mean, usually computed excluding tail values to account for anomalies (e.g., stray photons), is then subtracted from the raw image to remove any bias on the ADU values due to thermal noise. Typically, this subtraction is executed by the facility's software, as part of automatic post-processing. Additionally, it is now common for facilities to provide the detector images, with the background subtracted, in energy units. The ADU to energy unit conversion of detectors, i.e., $ADU_{sp}(E)$, is already regularly measured as part of performance testing and can automatically be applied to the raw ADU image in a post-processing step. However, in this article, we will always assume to work with background-subtracted images, but in ADU units, and we will show how to compute $ADU_{sp}(E)$ directly from the experimental images. While R_s is typically given in the camera documentation, accounting for the charge spread between pixels remains a task for the user as it is computationally quite intensive and not always necessary depending on the detector geometry or experiment. Finally, image post-processing often includes masking or correcting faulty pixels, with special attention to edge pixels, where leakage currents can reduce charge collection efficiency.⁴⁶

In the regions with low photon densities, which cover most of the detectors in our cases, we are able to identify a photon hit by searching clusters of neighboring pixels with ADU counts consistently above the noise. This technique, known as single photon counting, allows us to count the photons on the detector, thereby reducing the uncertainties in estimating N_{ij}^x by exploiting the spatial correlation between ADU values of neighboring pixels. The small regions with medium to high photon densities require instead more elaborated techniques to improve signal quality, which will be discussed in the following. Although it is possible to estimate the energy of the photon directly from the ADU count, as done in SPCS,^{34,47,48} working in dispersive (or Bragg) spectroscopy enables us to determine the energy of the photons by their positions, facilitating the use of the photon counting techniques.

B. Energy calibration

For both spectrometers of interest here, the energy map depends on the geometrical parameters of our setups (e.g., source-detector distance),

$$E_{ij} = E(x'_{ij}, y'_{ij}; \Lambda), \quad (1)$$

where x'_{ij} and y'_{ij} are the coordinates of the center of pixel (ij) on the planar detector and Λ collects all the geometrical parameters. These parameters will be used as fitting variables to find the energy map, ensuring that it is consistent with known experimental lines. Let us now separately examine two types of geometries that are commonly used, particularly in HED physics experiments.

1. Flat crystal spectrometer

We begin by assuming that the rocking curve of the reflecting crystal⁴⁹ is a Dirac delta centered at the Bragg angle, θ_B , and that the sample acts as a point source, thereby neglecting source broadening. Under these assumptions, using Bragg's law⁴⁹ and referring to Fig. 3, one can derive the following relation between E_{ij} , the coordinates of the pixel, and the geometrical parameters:⁵⁰

$$\begin{aligned} E_{ij} &= E(\theta_B(x'_{ij}, y'_{ij}; \Lambda)) \\ &= \frac{hc}{2d \sin(\theta_B(x'_{ij}, y'_{ij}; \Lambda))} \\ &= \frac{hc}{2d \hat{z} \cdot (\mathbf{r}_0 + \mathbf{R}\mathbf{r}'_{ij})}, \end{aligned} \quad (2)$$

where θ_B is the Bragg angle associated with pixel (i, j) , h is the Planck constant, c is the speed of light, and d is the spacing between the reflecting planes of the crystal. In this work, we consider the first-order reflection ($n = 1$), but the generalization of equations to any arbitrary order n is straightforward. The geometrical quantities \mathbf{r}_0 , \mathbf{r}'_{ij} , and \mathbf{R} are given by the following expressions (see Fig. 3):

$$\mathbf{r}_0 = D (\cos \bar{\theta}_B, 0, \sin \bar{\theta}_B), \quad (3)$$

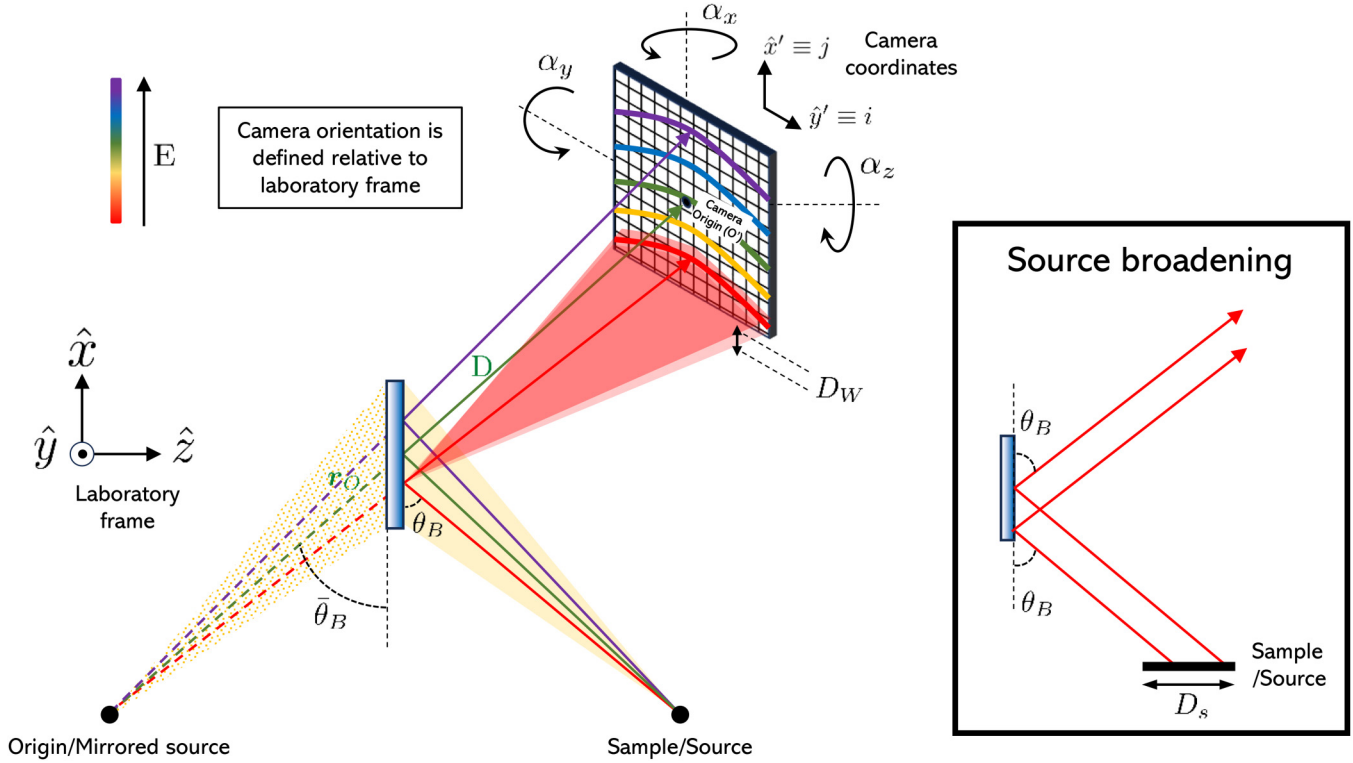


FIG. 3. Flat crystal (FC) spectrometer geometry with an illustration of source broadening (inset). The laboratory frame is defined by \hat{z} being the normal of the crystal, \hat{x} such that \mathbf{r}_0 is contained in the $\hat{x} - \hat{z}$ plane, and \hat{y} chosen for the frame to be an orthonormal right-handed triad. The camera frame is defined with \hat{x} and \hat{y} aligned with the pixel array, \hat{z} orthogonal to the camera plane, and the origin O' at the center of the detector.

$$\mathbf{r}'_{ij} = (x'_{ij}, y'_{ij}, 0), \quad (4)$$

$$\mathbf{R} = \mathbf{R}_x(\alpha_x)\mathbf{R}_y(\alpha_y)\mathbf{R}_z(\alpha_z). \quad (5)$$

Here, \mathbf{R} is the rotation matrix that specifies the orientation of the camera relative to the laboratory frame, parametrized with Euler's angles $(\alpha_x, \alpha_y, \alpha_z)$.⁵¹ Such angles, along with the distance D from the source to the camera origin O' and the Bragg angle θ_B associated with O' , constitute the geometrical parameters Λ for fitting and determining the energy map. In order to do this, we first identify, in terms of pixel coordinates, a bright curve S_{exp} on the experimental image A_{ij} associated with an emission line of known energy \bar{E} ,

$$S_{exp} = \{(i, f(i)), i = 1, \dots, N_y\} \text{ with } f(i) = \max_{N_1 \leq j \leq N_2} A_{ij}, \quad (6)$$

where N_1 and N_2 are appropriately chosen to isolate the emission line of energy \bar{E} . A more sophisticated and accurate method is to fit, for each row, the emission line to an analytic function and to take the peak of the fit as the line position. This approach is less susceptible to noise and allows for sub-pixel resolution, by constructing the energy map on a finer sub-pixel grid. However, for the purposes

of this paper, we adopt the method described by Eq. (6). As a second step, we compute the relative theoretical contour $\{(i, j) | E_{ij} = \bar{E}\}$ using Eq. (2) with a guess for Λ ,

$$S_{th}(\Lambda) = \{(i, g(i; \Lambda)), i = 1, \dots, N_y\} \quad (7)$$

with $g(i; \Lambda) = \min_j |E_{ij}(\Lambda) - \bar{E}|$.

S_{exp} and S_{th} are parametrized with i as the independent variable because of the expected shape for these curves. Finally, we calculate a loss function \mathcal{L} , dependent on the geometrical parameters Λ , measuring a distance between the experimental line S_{exp} and the theoretically computed contour S_{th} ,

$$\mathcal{L}(\Lambda) = \frac{1}{N_y} \sum_{i=1}^{N_y} (f(i) - g(i; \Lambda))^2. \quad (8)$$

At this point, we can minimize \mathcal{L} over the space of the geometrical parameters with standard optimization routines.⁵² The loss function can include multiple emission lines by summing the loss functions of each individual line, as previously defined. This

summation can include different weights for each line, proportional to their intensities. Figure 4 illustrates an example of this calibration for the Mg spectrum discussed earlier. Here, the geometrical parameters of the setup are determined by fitting the Mg $K\alpha$ line and are found to be

$$\begin{aligned}(\alpha_x, \alpha_y, \alpha_z) &= (-1.9^\circ, 55.8^\circ, 0^\circ) \\ D &= 79.5 \text{ mm} \\ \bar{\theta}_B &= 34.7^\circ.\end{aligned}\quad (9)$$

As we see from these values, it is common practice to work with the camera orthogonal to \mathbf{r}_0 in order to maximize the solid angle coverage of the detector, as well as to minimize any grazing incidence broadening in the sensor layer (see Sec. II B 3). In this work, we disregard the uncertainties in the Λ parameters arising from the fitting process, as their impact on the final energy map is minimal. This is justified by the fact that these errors are typically small, especially when multiple emission lines are used for fitting. Consequently, their contribution to the energy map uncertainties is negligible compared to the broadening effects discussed in Sec. II B 3.

2. Von Hámos spectrometer

In the von Hámos (VH) geometry,⁵³ an axis (the dispersion axis) is drawn between the source and the detector, and the detector surface lies along this line (see Fig. 5). A cylindrically bent crystal is then placed parallel to this axis, with the crystal positioned at its radius of curvature below this axis. The crystal will, therefore, focus the reflected rays back on to the dispersion axis at a distance twice as far away in the dispersive direction. This results in a simple dispersion relationship between the photon energy E , the position from the source to the front of the camera along the

dispersion axis L , and the position on camera along the dispersion axis X_{cam} ,

$$E = \frac{hc}{2d} \sqrt{1 + \frac{(L + X_{\text{cam}})^2}{4R^2}}, \quad (10)$$

where R is the radius of curvature of the crystal, and the remaining symbols have the same meaning as before. The calibration is straightforward and involves the optimization of R and L using analogous techniques to those described for the flat crystal geometry. Bright emission lines with known energies are well-suited to this task. Two sets of lines that cover the detector range are ideal for the calibration and should result in a very well-constrained dispersion relationship. We show an example of an experimental calibration in Fig. 6.

The primary benefit of a von Hámos spectrometer is its collection efficiency. By focusing all the rays onto a single axis instead of arcs as with the flat crystal spectrometer, it is easier to detect events above the noise. As the bending process deforms the lattice of a perfect crystal, its rocking curve becomes extended, which degrades the intrinsic resolution of the crystal.^{55,56} It is, therefore, common to use mosaic crystals as the dispersive crystal to further increase the collection efficiency of the spectrometer. Common examples of such crystals are highly annealed pyrolytic graphite (HAPG), highly oriented pyrolytic graphite (HOPG), and lithium fluoride (LiF). A mosaic crystal is one that consists of small perfect crystallites with their normal vectors randomly distributed around the crystal surface normal. As a result, in contrast to perfect crystals where reflections only take place around the Bragg angle within the rocking curve, the Bragg condition can be satisfied anywhere on a mosaic crystal by finding a crystallite appropriately angled to the normal (see Fig. 5). This effect increases the area of the crystal reflecting a certain photon energy on a specific spot of the detector (mosaic focusing). The end result is that von Hámos spectrometers have very high collection efficiencies and so are often employed in situations where photon numbers are very low, such as in x-ray Thomson scattering (XRTS) and resonant inelastic x-ray scattering experiments.^{54,56}

As the x rays are focused onto the dispersion axis, the spectrum is produced by integrating over a few pixels along the non-dispersive direction. The number of pixels used is chosen to maximize the signal-to-resolution ratio (see Ref. citenumpreston). Outside this region of interest (RoI), unfocused x rays are disregarded, as different photon energies overlap on the same pixels.

The drawback to mosaic crystal VH spectrometers is that their resolution tends to be worse than for flat crystal spectrometers. The bulk of this is due to the mosaicity of the crystal, which both enhances depth broadening and itself contributes directly to the broadening. As a result, photons of a specific energy are sent to different locations on the detector rather than to a precise, nominal point, producing a non-trivial broad and extended instrument function.⁵⁷ Furthermore, the mosaicity causes broadening in the non-dispersive direction, resulting in a characteristic X-shaped instrument function across the detector, with wider crystals producing a more extreme shape.^{59,60} This broadening leads to the aforementioned energy mixing outside the central RoI. If the

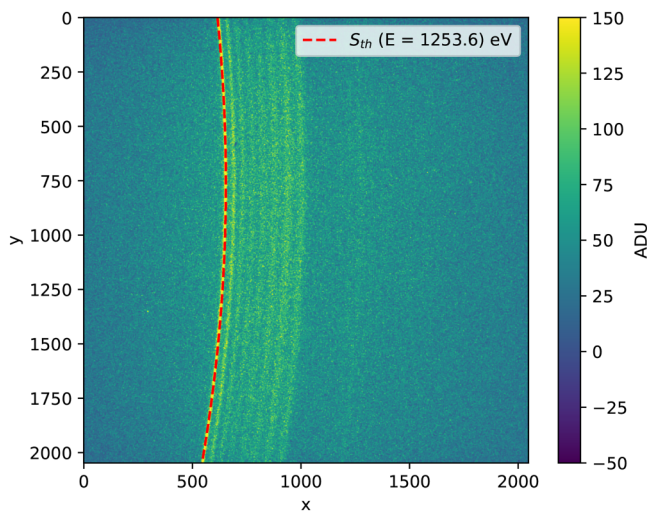


FIG. 4. Detector image of MgF_2 emission spectrum with the theoretically computed energy contour (red) fitted to a Mg $K\alpha$ line.

10 April 2025 18:02:44

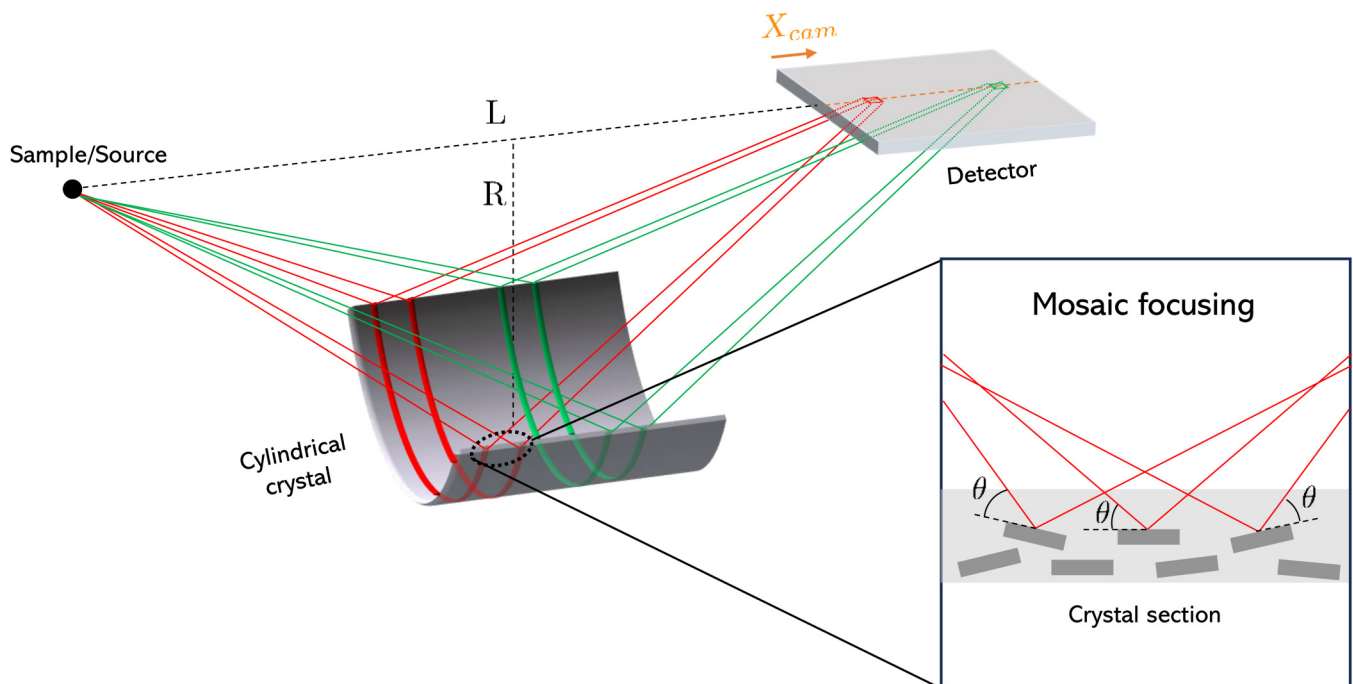


FIG. 5. Von Hámos spectrometer setup with an illustration of mosaic focusing (inset). The mosaicity of the crystal increases the area that reflects a certain photon energy. For the correct functioning of the spectrometer, the crystal must be placed halfway between the source and the center of the detector. As in the flat crystal case, θ_B is defined as the Bragg angle associated with the center of the detector.

spectrometer lies slightly out of focus, the broadening in the non-dispersive direction can become curved, in either direction, depending on the vertical position of the crystal and its various physical properties such as mosaicity. Indeed, we observe this sort of defocusing in the energy contours (Fig. 6), where emission lines show a backward sweep.

Focal aberrations are in fact an additional factor that can degrade resolution,⁵⁹ but this effect can be reduced by using a relatively narrow crystal.^{58,59} Typical resolutions of von Hámos spectrometers range from 1 to 10 eV.^{58,61,62}

3. Broadening effects

The energy of each photon should map precisely to a corresponding position on the detector. In practice, however, various broadening mechanisms can cause photons of the same nominal energy to be recorded at different locations on the detector. As the spectrometer is calibrated so that spatial points on the detector correspond to specific energies, there is no way to distinguish between a photon arriving at its nominal position, and a photon with a different energy landing at the same point due to some broadening effect. This effect is described by a point spread function, also known as an instrument function (IF), and results in the observation of broadened features and a loss of spectral resolution.

While high-resolution spectra are generally desirable, there is a trade-off between resolution and signal intensity as the very

effects that result in broadening also tend to result in higher spectrometer efficiencies. For example, a broader rocking curve reduces resolution but increases crystal reflectivity, while a larger pixel size leads to greater quantization errors yet allows more photons to be detected by a single pixel, yielding a better SNR.

Broadening effects are generally complex to account for, as the instrument function (IF) can be strongly geometry-dependent and varies between experiments and setups. Furthermore, the IF rigorously depends also on the photon energies incident on the crystal.⁵⁷ In other words, the broadening of the spectrum due to IF cannot be expressed as a simple convolution but must be formulated as a Fredholm integral equation (FIE),

$$I(E) = \int K(E, E_0) I_{\text{orig}}(E_0) dE_0, \quad (11)$$

where I and I_{orig} represent the measured and original spectra, respectively, and the kernel $K(E, E_0)$ is the energy-dependent instrument function. Methods for determining K are outlined in Ref. 57 and rely on a combination of quasi-elastic signal measurements and theoretical modelling of the IF. Once K is known, I_{orig} can be retrieved using standard techniques for solving FIEs. Even in cases where the dependence of IF on the incident energy could be neglected—making the calculation of I_{orig} a simpler deconvolution problem—finite spectral windows and experimental noise

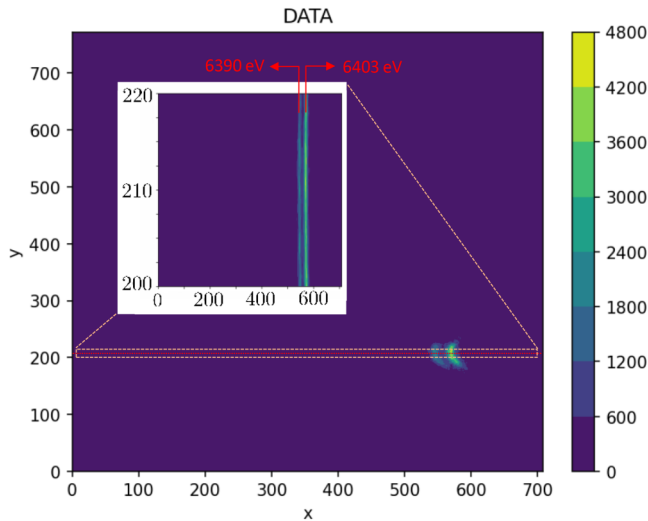


FIG. 6. Detector image of Fe emission using a von Hámos spectrometer from the experiment reported in Ref. 55, with a zoomed inset around the central dispersion axis, indicated by the red dotted line. The two vertical bright lines in the inset correspond to the isoenergy contours of the Fe K-alpha lines. Generally, the central dispersion axis may be slightly tilted relative to the detector's edge. This tilt is accounted for by adjusting the region of interest while moving along the dispersive direction. However, Eq. (10) remains valid, as corrections due to the tilt are typically negligible.

introduce instability in the deconvolution process. As a result, a small amount of noise in I can cause significant distortions in I_{orig} .

We list the main effects that deteriorate the resolution of the measured spectra.

- **Finite pixel size and quantization error:** Pixels are rectangles with sides of finite length L_p , causing each pixel to collect photons within an energy range of order $O(\frac{2hc \cos \theta_B}{d \sin^2 \theta_B} \frac{L_p}{D})$. The energy calibration of a pixel E_{ij} thus represents an average energy. For the cameras used in the experiments, typical L_p values are in the range of $\sim 10\text{--}100 \mu\text{m}$,⁶³ which is generally sufficiently small to measure a smooth spectrum with energy bins of $\leq 2 \text{ eV}$. The energy bin width ΔE must be chosen as small as possible to reduce the quantization error ($\sim \Delta E/\sqrt{12}$) but large enough to contain several E_{ij} in order to obtain smooth spectra. As an aside, there is a trade-off to be considered in pixel size—while smaller pixels will have less pixel broadening, they also suffer from increased charge spreading between pixels. If the charge of a photon is spread between too many pixels, it may become difficult to detect signal above the noise. As a result, there is a balance between the possible energy bin size and the ability to reliably detect photons above the noise. These two broadening effects, unlike the ones discussed next, degrade resolution without affecting the correspondence between photon energy and its position on the detector.
- **Source broadening (SB):** As the incident beam has a finite size, photons leave the target from a region on the sample with an

effective size D_s , typically ranging from several nm to dozens of μm , and up to hundreds of μm for synchrotron and laser-plasma-based sources. This region is often approximated as a circle, although imprints of the beam show that the laser spatial profile can be more complex.⁶⁴ Additionally, as samples have finite thickness, photons also emerge from different points from within the sample. Consequently, photons of the same energy emitted from different points in the sample will reach the detector at different points, representative of the shape of the source, which results in photons of different energies landing on the same point, broadening the measured spectrum (see Fig. 3). The energy uncertainty on each pixel, due to this effect, is of order $O(\frac{2hc D_s \cos \theta_B}{d D})$.

- **Depth Broadening (DB):** A photon can travel a finite depth into a crystal before being reflected out again. As a result, it reflects at a point displaced from the nominal position it would reflect from on the surface and will, therefore, hit the detector at a different point. The DB resembles an exponential function as it represents the probability a photon reflects from a certain depth in the crystal. For perfect crystals, this is typically a very narrow function and does not contribute significantly to the broadening. However, for mosaic crystals, the broadening can be substantial (several eV) due to the distribution of the crystallites³⁷ and is made even broader by non-negligible multi-reflection paths within the crystal.⁶⁵ When the path travelled inside the crystal is much smaller than its attenuation length—a necessary condition to maintain the crystal's reflectivity—the SB is proportional to $t/\sin(\theta_B)$, with t representing the crystal thickness. Since t cannot be reduced excessively without compromising reflectivity, it is important to avoid working at overly shallow incidence angles. The same consideration applies to the detector, where small incidence angles influence the depth and, depending on L_p , the pixel position of the photoabsorption, thereby impacting pixel detection and increasing charge spreading.⁶⁷
- **Finite width of the rocking curve:** Another source of energy broadening is the finite width of the crystal rocking curve (RC), D_W , which can be computed using dynamical diffraction theory.⁴⁹ The RC allows for a photon that does not satisfy the Bragg condition to nevertheless be reflected from the crystal,⁴⁹ albeit with a lower probability. For perfect crystals, their intrinsic RC can be calculated using dynamic diffraction theory, and it is an extremely narrow function.⁴⁹ Typical values for D_W are dozens of μrad . For mosaic crystals, the mosaic distribution of the crystallites also contributes to the RC and is about an order of magnitude larger than the intrinsic RC of the crystallites.⁶⁷ The energy uncertainty per pixel from this effect is then simply of order $O(\frac{2hc}{d} D_W)$. D_W is generally weakly dependent on the photon energy⁶⁷ and is often assumed to be constant for typical spectrometer energy windows.

For the geometrical setup of the Mg experiment, summarized by Parameters (9), with typical values for L_p , D_s , and D_W , the energy resolution losses produced by these effects are of around $0.5\text{--}1 \text{ eV}$. In many scientific fields, these resolution losses are of secondary importance, as other factors such as source bandwidth dominate.⁶⁸ Nevertheless, they must be considered if one wants to reach high resolutions (sub-eV). These resolutions can be achieved

10 April 2025 18:02:44

by means of specific experimental setups, characterized by large source–detector distances and high resolution crystals with very narrow RC.^{69,70} However, these features also tend to decrease the SNR of the images. It is, therefore, useful to contrive alternative methods that mitigate these resolution losses, without compromising the signal intensity. One potential solution to overcome the resolution limitations imposed by the finite pixel size is to analyze the charge distribution between neighboring pixels. Techniques used to manage charge spreading, based primarily on centroid calculations, have been successfully employed in the past to handle such correlations and achieve sub-pixel resolutions.^{40,41} Nevertheless, it is important to note that these methods are applicable only when the pixel dimensions are sufficiently small compared to R_s and in low photon-density regimes. In Sec. II D, we will introduce an alternative approach to treat these correlations, based on deconvolution algorithms capable of also handling cases with large photon densities on the detector.

The remaining three effects can be mitigated by studying the instrument function of the experimental setup and solving the involved integral equation mentioned earlier. Assuming the pixel size effect to be negligible or already accounted for, we can study the broadening due to the spectrometer instrument function by irradiating the target with a monochromatic source and compare the elastic scattering measured on the spectrometer to a high-resolution beam spectrometer.⁵⁷ For this method to work, a material with very weak inelastic scattering in the vicinity of the elastic scattering must be chosen. Good choices include plastics such as polymethyl methacrylate and polypropylene, or metallic glasses.^{57,71} Another common way to determine the resolution of a setup is from emission lines with known line shapes, e.g., Hölzer *et al.*'s 3d metal transition lines.⁷² In any case, the FWHM of the instrument function used provides an estimate of the spectrometer resolution.

C. Experimental estimation of camera parameters

A fundamental quantity for converting the ADU map to the distribution of photon hits is the RMS of the camera read noise, σ_N , which measures the level of thermal noise in the detector. This can be measured pixel-wise by running the camera without a source and calculating the variance of the pixel values during these dark runs. However, for simplicity, we will consider this quantity to be constant across the camera, which is a reasonable approximation for the typical detectors employed.^{63,73} In these cases, σ_N is directly inferable from the histogram of the camera images with signal present, the shape of which we will now discuss.

We will assume the detector images have undergone dark image subtraction, so that the expected value of the ADU count for a pixel not hit by any photon is zero. Additionally, for our cases, the analysis of the histogram is simplified because, in Bragg spectroscopy, photon energies are determined by their position on the detector. Consequently, we can subdivide the camera into regions (e.g., rectangles that tile the entire camera) sufficiently small to approximate $ADU_{sp}(E)$, the ADU counts produced by a photon of energy E , as constant (ADU_{sp}) in each region. The shape of the histogram for a single region is in general a series of peaks centered

approximately in the following sequence of values:

$$P_n = \zeta \cdot n \cdot ADU_{sp}, \quad n = 0, 1, 2, \dots, \quad (12)$$

where ζ is a constant smaller than 1 (typically around 0.8–0.9), whose origin will be discussed below. The n th peak contains the pixels that are likely to have been hit by n photons. In reality, only the initial peaks of this sequence will appear in the histogram, depending on the density of photon hits, which is measured by the so-called fill fraction λ . This important parameter is defined as

$$\lambda = \frac{\# \text{ photons on the camera}}{\# \text{ pixels in the camera}}. \quad (13)$$

Each peak is broadened by the intrinsic noise of the detector and the charge spreading, quantified by σ_N and R_s , respectively. The magnitude of these broadening effects determines whether the peaks will be merged together or remain distinct. Additionally, charge spreading systematically shifts the peaks, initially centered at $nADU_{sp}$, toward lower ADU values, as some of the photon energy is deposited across multiple pixels. The constant ζ in Eq. (12) accounts for this shift, decreasing as R_s increases. To illustrate these effects, in Figs. 7(a)–7(d), we present histograms generated from synthetic camera images with various levels of noise and fill fractions. More details on the fabrication of these synthetic images are provided in Sec. III A. Alongside these synthetic data, we include an experimental histogram for MgF₂ in Fig. 7(e) for data from Ref. 23.

If $ADU_{sp}(E)$ is not provided by the facility, it can be directly inferred from the position of the first peak in the series given by Eq. (12), which corresponds to single photons hitting pixels on the camera. Similarly, from the width of the peak centered around 0, we can estimate σ_N . Intuitively, the more the peaks merge together, the more challenging it becomes to accurately determine these quantities. In such cases, one approach to extract these two parameters is to fit the experimental histograms to a theoretical model. This model can be constructed (see Sec. III A) given certain values for ADU_{sp} , σ_N , and λ , which can be estimated from the expected number of photons, and R_s , usually provided in the camera documentation.

D. Estimate of the photon hits distribution

The objective of this section is to describe how to compute the distribution of photon hits, N_{ij}^p , from the camera image A_{ij} , thereby eliminating the distortions due to thermal noise and charge spreading. Depending on the spectrum of photons hitting the camera, the image will have regions with different local fill fractions (see Fig. 11), which must be treated with distinct methods. Therefore, to process the image, we apply the following two techniques:

- (1) **Photon counting algorithms:** To address regions with small fill fractions ($\lambda \lesssim 0.1$), where single photon clusters are present, we use photon counting algorithms. These algorithms can identify single photon clusters, exploiting the correlation between neighboring pixels to reduce the uncertainty on the photon detection.

10 April 2025 18:02:44

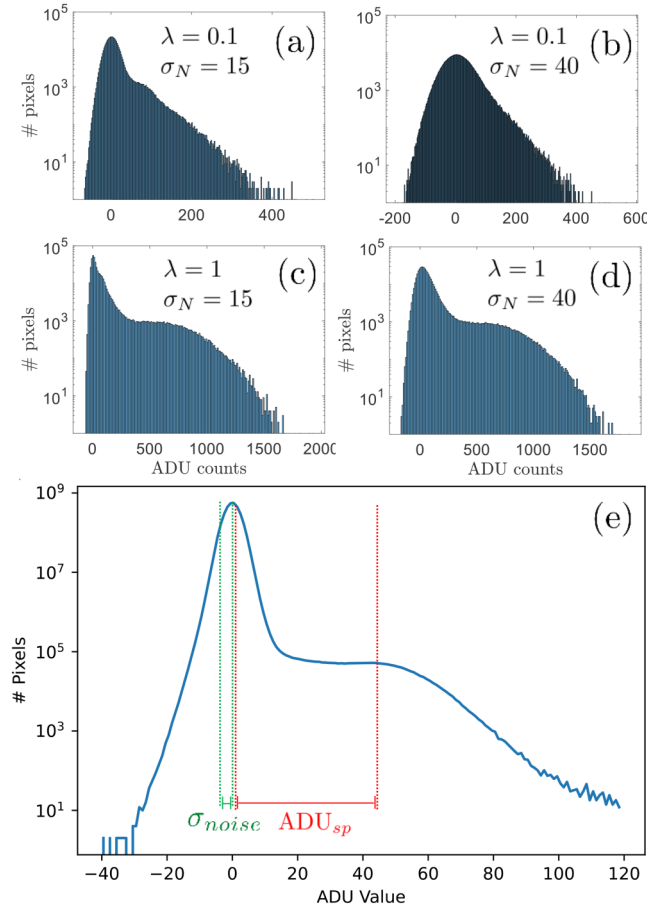


FIG. 7. (a)–(d) Synthetic histograms of 700×700 images for various levels of noise and fill fractions. ADU_{sp} is taken equal to 120. (e) Histogram of the camera image reported in Fig. 1.

- (2) **Image deconvolution techniques:** To treat the regions with large fill fractions ($\lambda \gtrsim 1$), where agglomerated clusters are present (see next section), we process the image with the Richardson–Lucy deconvolution method.⁷⁵

As we will see, these two operations can be carried out sequentially, improving the signal quality across the entire range of λ , including also intermediate fill fractions. Considering the discussion in Sec. II C, we will assume in the following that the camera parameters ADU_{sp} , σ_N , and R_s are known.

1. Clustering algorithms

If we suppose, as is often the case, that the charge produced by a photon does not spread further than a pixel side length, then the shapes of single-photon clusters (i.e., the pixels in which the charged produced by the photon has leaked) are few and given in Fig. 8. As there are only 13 possible shapes, a simple clustering algorithm can be employed to identify these clusters and

re-accumulate the intensity back on to the central pixel. The benefit of doing so is that this makes the pixel brighter relative to the background, allowing for more of these events to be included once the final thresholding is performed.

The first step to identify the photon hits from the ADU map is thresholding the camera image. Although different choices are possible for the thresholding value, here, we chose $1.5 \sigma_N$, as a good compromise to cut the noise and retain the signal,

$$A_{ij}^{th} = \begin{cases} A_{ij} & A_{ij} \geq 1.5 \sigma_N \\ 0 & A_{ij} < 1.5 \sigma_N \end{cases} \quad (14)$$

The thresholding value can be chosen in a systematic way by analyzing their performance over multiple synthetic images for a given set of parameters (ADU_{sp} , σ_N , and R_s). This method is briefly described in Appendix A. After thresholding, the pixels with an ADU value different from zero are the ones that most likely received a contribution to their ADU by a photon hit. One may also set pixels exceeding some upper threshold to zero to mask out possible faulty pixels or high intensity events that do not correspond to real signal.

Next, we locate any clusters and determine whether they fall into one of two cases:

- (1) **Single-photon clusters.** If the shape of the cluster C matches that in Fig. 8, then the charge spread is considered to originate from the brightest pixel, and we accumulate all the ADU values of the cluster onto its brightest pixel (\bar{i}, \bar{j}),

$$A'_{\bar{i}, \bar{j}} = \sum_{(i,j) \in C} A_{ij}^{th} \quad (15)$$

$$A'_{ij} = 0 \text{ for } (i, j) \in C \text{ and } (i, j) \neq (\bar{i}, \bar{j}).$$

- (2) **Agglomerated clusters.** In this case, we do not modify the ADU values,

$$A'_{ij} = A_{ij}^{th}. \quad (16)$$

After the clustering algorithm is applied, the image is thresholded once more with a higher threshold, assuming that any events that fall below the threshold did not originate from a single photon event. For this work, we choose $(ADU_{sp} - \sigma_N)$ as the second threshold, which results in discarding roughly 20% of the single photons (A'_{ij} has a larger variance than A_{ij}) but eliminates almost entirely noise fluctuations. This second threshold can also be systematically determined using the method outlined in Appendix A. Charge accumulation over the brightest pixel can also be carried out by considering the centroid of the single-photon cluster, enabling subpixel resolution.⁴⁰ However, this more advanced process is beyond the scope of our discussion here.

In Fig. 9, we report an example of this operation using a synthetic camera image (see Sec. III A for more details). As is observed, agglomerated clusters remain unchanged by this algorithm and will be addressed in Sec. II D 2.

Exploiting the correlation of ADU values across neighboring pixels enables us to boost the signal. As an example, consider three adjacent pixels arranged in an L-shape, with ADU values between

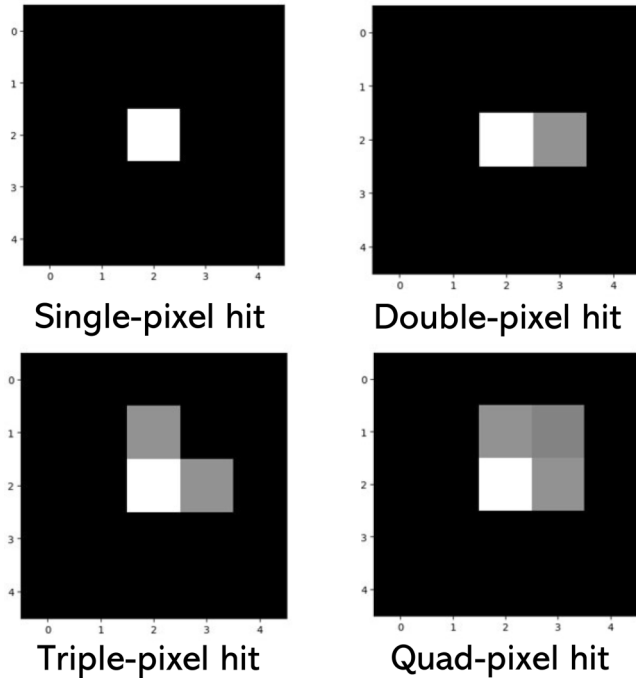


FIG. 8. The four layouts for a single photon cluster. The brighter pixel represents the pixel hit by the photon. Each of the last three can rotate by 90° , 180° , and 270° to produce 13 layouts in total.

the first and second thresholds. If the correlation is ignored and, consequently, we do not accumulate the ADU values on the brightest pixel, all three pixels will be zeroed after the second thresholding, resulting in a loss of signal that likely corresponds to a photon. In fact, a simple analysis shows that it is significantly more likely that three L-shaped pixels with values above $1.5\sigma_N$ are caused by a photon compared with noise.

In addition to this, thresholding mitigates noise-related fluctuations in the reconstructed spectrum. The noise reduction is approximately proportional to $\mathcal{P}(N_{ij}^\gamma \geq 1) < 1$, where $\mathcal{P}(N_{ij}^\gamma \geq 1)$ is the probability that at least one photon lands on pixel (i, j) . This result can be derived by considering the variance of the random variables $A_{ij} \approx N_{ij}^\gamma \text{ADU}_{sp} + \eta_{ij}$ (see Appendix B) and A_{ij}^{th} (as defined earlier), where η_{ij} represents the random noise on pixel i, j , which is assumed to be Gaussian-distributed with mean 0 and variance σ_N : $\eta_{ij} \sim \mathcal{N}(0, \sigma_N)$. First, fixing the number of photons N_{ij}^γ , we find

$$\begin{aligned} \mathbb{V}(A_{ij}|N_{ij}^\gamma) &= \mathbb{V}(\eta_{ij}) = \sigma_N^2 \quad \forall N_{ij}^\gamma, \\ \mathbb{V}(A_{ij}^{th}|N_{ij}^\gamma) &= \begin{cases} \sigma_N^2 & A_{ij} \geq \kappa\sigma_N \\ 0 & A_{ij} < \kappa\sigma_N, \end{cases} \end{aligned} \quad (17)$$

where $\mathbb{V}(\cdot)$ represents the variance and $\kappa\sigma_N$ is a generic threshold proportional to σ_N . Now, taking the mean values \mathbb{E} over the

random variable N_{ij}^γ , we obtain

$$\begin{aligned} \mathbb{E}(\mathbb{V}(A_{ij})) &= \sigma_N^2 \mathcal{P}(N_{ij}^\gamma = 0) + \sigma_N^2 \mathcal{P}(N_{ij}^\gamma = 1) + \dots = \sigma_N^2, \\ \mathbb{E}(\mathbb{V}(A_{ij}^{th})) &= 0 \cdot \mathcal{P}(N_{ij}^\gamma = 0) + \sigma_N^2 \mathcal{P}(N_{ij}^\gamma \geq 1) < \sigma_N^2, \end{aligned} \quad (18)$$

having taken as an approximation that $\mathcal{P}(A_{ij} < \kappa\sigma_N | N_{ij}^\gamma > 1) = 0$ and $\mathcal{P}(A_{ij} > \kappa\sigma_N | N_{ij}^\gamma = 0) = 0$. Summing the ADU values over the energy contours preserves the ratio between the variance of the raw and thresholded values.

2. Images deconvolution

To address charge spreading and noise contributions in regions with large λ , we apply the Richardson–Lucy (RL) deconvolution algorithm⁷⁴ to the matrix A'_{ij} . This method is an iterative procedure, based on Bayesian inference, that computes the most likely expected values V_{ij} of the Poissonian and independent variables X_{ij} , given a realization R_{ij} , which has been blurred out by a known kernel function H and corrupted by random noise. In formulas,

$$\begin{aligned} R_{ij} &= (X * H)_{ij} + \eta_{ij}, \\ X_{ij} &\sim \text{Poisson}(V_{ij}), \quad \eta_{ij} \sim \mathcal{N}(0, \sigma_N^2), \\ R_{ij} &\xrightarrow{\text{RL algorithm}} V_{ij}, \end{aligned} \quad (19)$$

where $*$ denotes the convolution symbol and X_{ij} and η_{ij} are uncorrelated random variables for each i and j . It is intuitive to see that this problem is analogous to our case, where X_{ij} is the number of photons landing on pixel ij , V_{ij} is the intensity of the spectrum at that pixel energy $I(E_{ij})$, H is an effective charge spreading function (defined in Appendix B), η_{ij} is the thermal noise on pixel ij , and R_{ij} is the ADU map. Therefore, defining A_{ij}^{proc} as

$$A'_{ij} \xrightarrow{\text{RL algorithm}} A_{ij}^{proc}, \quad (20)$$

it will constitute an estimate for $I(E_{ij})$, which is the quantity we are interested in. A more rigorous justification for the application of this method is presented in Appendix B.

In Fig. 9(d), we illustrate the result of applying the RL algorithm to the camera image already treated with the photon counting algorithms. As observed, the algorithm decomposes the agglomerated clusters into the most likely distribution of photon hits (still in ADU units), leaving the single-photon clusters unchanged. The comparison between the reconstructed map A_{ij}^{proc} and the original photon hits is excellent, with only very few mismatches.

Finally, we convert the camera units to photon numbers, which provides the intensity in the measured spectrum,

$$N_{ij}^\gamma = \frac{A_{ij}^{proc}}{\text{ADU}_{sp}}. \quad (21)$$

E. Construction of the spectrum and solid angle corrections

The final step is to construct an estimate of the photon emission spectrum, $S(E)$, in the direction of the detector, based on the

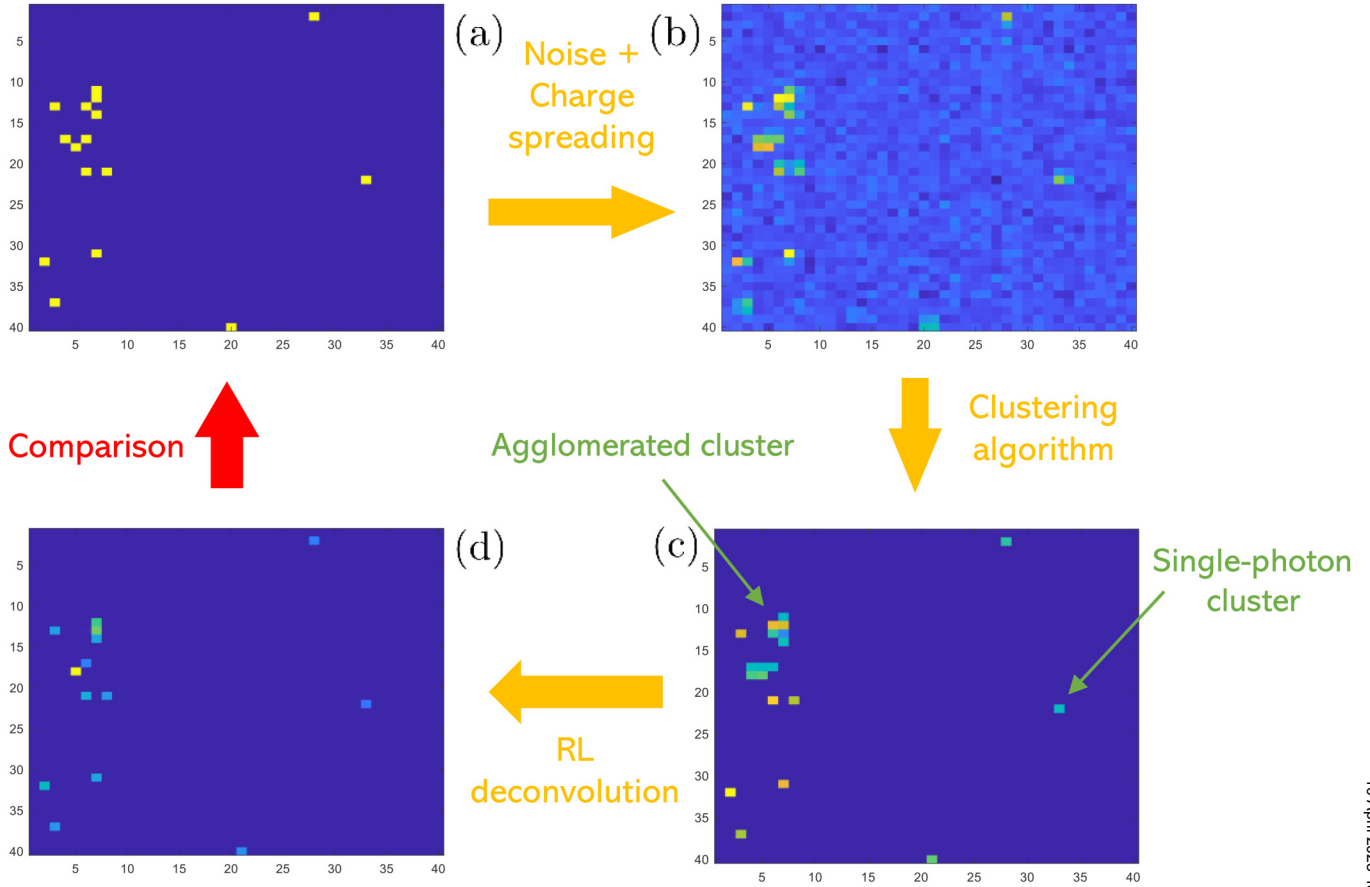


FIG. 9. Illustration of the various steps in the camera image processing. (a) Map of photon hits on the camera for a small λ , to which thermal noise and charge spreading have been applied to obtain the camera image (b). The same image processed with the clustering counting algorithm (c) and then with the deconvolution algorithm (d). In the figure, we indicate an example of a single-photon cluster and of an agglomerated cluster. All camera images, except the first initial photon map, are in ADU units.

photon hit distribution N_{ij}^{γ} obtained in Sec. II D. In the following, we will assume the emission spectrum to be independent of the unit direction $\hat{\mathbf{k}}$ in the solid angle detected by the camera Ω_{det} . If this assumption does not hold, the following discussion remains largely unaffected, except that the calculated spectrum will represent values averaged over all detected directions for a given energy. $S(E)$ describes the probability that, given a source spectrum, a photon of energy E will be scattered in the direction observed by the camera. Its units are $\text{sr}^{-1}\text{eV}^{-1}$. The measured spectrum $I(E_l)$, which represents the probability of detecting a photon within a given energy interval, can then be expressed as follows:

$$I(E_l) = \int_{\Omega_{det}} d\Omega(\hat{\mathbf{k}}) \int_{E_l - \Delta E/2}^{E_l + \Delta E/2} dE S'(E, \hat{\mathbf{k}}) \quad (22)$$

$l = 1, \dots, N_b,$

where E and $\hat{\mathbf{k}}$ are the energy and unit wave vector of the photons, ΔE is the energy resolution, and N_b is the number of energy bins. Here, $S'(E, \hat{\mathbf{k}})$ is the emission spectrum $S(E)$ modified by the action

of the Bragg crystal, summarized in the shape function $F(E, \hat{\mathbf{k}})$,

$$S'(E, \hat{\mathbf{k}}) = S(E)F(E, \hat{\mathbf{k}}). \quad (23)$$

Integrating Eq. (22) over the energies, we obtain

$$I(E_l) = \int_{\Omega_{det}} d\Omega(\hat{\mathbf{k}}) \bar{S}'(\hat{\mathbf{k}}; E_l). \quad (24)$$

Given the energy-dispersive effect of the crystal on the radiation and assuming that crystal broadening (including depth and mosaicity effects) is sufficiently small, $\bar{S}'(\hat{\mathbf{k}}; E_l)$ can be approximated in the following way:

$$\bar{S}'(\hat{\mathbf{k}}; E_l) = \bar{S}(E_l) = \int_{E_l - \Delta E/2}^{E_l + \Delta E/2} dE S(E) \quad (25)$$

$$\forall k \mid E_l = \arg \min_{E_{ij}} |E(\hat{\mathbf{k}}) - E_{ij}|$$

and equal to zero for all the other values of $\hat{\mathbf{k}}$. Here, $E(\hat{\mathbf{k}})$ is given by Eq. (2), with

$$\hat{\mathbf{k}} = \frac{\mathbf{r}_0 + R\mathbf{r}'}{\|\mathbf{r}_0 + R\mathbf{r}'\|}, \quad \mathbf{r}' = (x', y', 0). \quad (26)$$

Now, the integration over the solid angle in Eq. (24) becomes

$$I(E_l) = S(E_l) \cdot \sum_{ij|E_{ij} \in \Delta(E_l)} \Omega_{ij}. \quad (27)$$

Having denoted the interval $(E_l - \Delta E/2, E_l + \Delta E/2)$ as $\Delta(E_l)$ and Ω_{ij} the solid angle associated with pixel ij . This solid angle for the flat crystal spectrometer can be computed through the following formulas:

$$(\hat{\mathbf{z}}')_{\text{lab}} = R(\hat{\mathbf{z}}')_{\text{cam}} \quad \text{with} \quad (\hat{\mathbf{z}}')_{\text{cam}} = (0, 0, 1), \quad (28)$$

$$\mathbf{x}_0 = \hat{\mathbf{z}}'(\hat{\mathbf{z}}' \cdot \mathbf{r}_0) \quad \text{with} \quad (\mathbf{r}_0)_{\text{lab}} = D(\cos \bar{\theta}_B, 0, \sin \bar{\theta}_B), \quad (29)$$

$$|\mathbf{x}_0| = |\hat{\mathbf{z}}' \cdot \mathbf{r}_0| = D' \rightarrow (\mathbf{x}_0)_{\text{cam}} = (0, 0, D'), \quad (30)$$

$$\mathbf{x}'' = \mathbf{r}_0 - \mathbf{x}_0 + \mathbf{x}' \rightarrow (\mathbf{x}'')_{\text{cam}} = (x'', y'', 0), \quad (31)$$

$$\text{with } (\mathbf{r}_0)_{\text{cam}} = R^{-1}(\mathbf{r}_0)_{\text{lab}} \quad \text{and} \quad (\mathbf{x}')_{\text{cam}} = (x', y', 0), \quad (32)$$

$$\mathbf{x} = \mathbf{x}_0 + \mathbf{x}'' \rightarrow (\mathbf{x})_{\text{cam}} = (x'', y'', D'), \quad (33)$$

$$\Omega(x, y) = \frac{dx dy \cos(\beta)}{|\mathbf{x}|^2} = \frac{dx dy |\mathbf{x}_0|}{|\mathbf{x}|^3} = \frac{D'}{(x''^2 + y''^2 + D'^2)^{3/2}}, \quad (34)$$

where the relative quantities are defined in Fig. 10. Similar reasoning can be carried out for computing the solid angles in the von Hámos geometry.

The intensity $I(E_l)$ can be estimated (see Appendix C) from the distribution of photon hits N_{ij}^y as

$$\tilde{I}(E_l) = \sum_{ij|E_{ij} \in \Delta E_l} N_{ij}^y. \quad (35)$$

Putting Eqs. (27) and (35) together, we obtain an estimate $\tilde{S}(E_l)$ for the emission spectrum,

$$\tilde{S}(E_l) = \frac{\sum_{ij|E_{ij} \in \Delta E_l} N_{ij}^y}{\sum_{ij|E_{ij} \in \Delta(E_l)} \Omega_{ij}} = \frac{\tilde{I}(E_l)}{\Omega(E_l)}. \quad (36)$$

When summing the number of photons over the energy contours associated to these bins, we will reduce the fluctuations due to the thermal noise and Poissonian statistics, thanks to the large numbers of pixels.

III. RESULTS

In this section, we apply the discussed methods to both synthetic and experimental data. The synthetic data will be utilized to evaluate the algorithms' performance in enhancing resolution and SNR for different conditions. The experimental data will instead demonstrate how these methods can amplify specific spectral features that would otherwise be weak, showcasing the efficacy of these techniques in real situations.

A. Synthetic data

In order to test our techniques, we generated some artificial camera images through the following steps, further illustrated in Fig. 11:

- (1) We create a 40×40 array to represent the camera pixels and a finer 4000×4000 subgrid to depict its surface. For simplicity, the energy contours on the camera are vertical, corresponding to the columns of the pixel matrix.
- (2) A number of photons, specified by the selected λ , are sent onto the subgrid. Their energy, which determines the pixel column they land on, is sampled from the spectrum $S(E_l)$ shown in Fig. 11(a) and then converted to an ADU value, taking $\text{ADU}_{sp} = 120$.
- (3) Charge spreading is applied by convolving the subgrid image with a gaussian kernel of width R_s . The ADU values of the subgrid belonging to the same pixel are then summed together to obtain the actual camera image [see Fig. 11(c)].
- (4) Finally, gaussian random noise with standard deviation σ_N is added to the image [Fig. 11(d)].

We evaluated the performances of our techniques for different values of λ , R_s , and σ_N by computing the \mathcal{L}_2 distance between

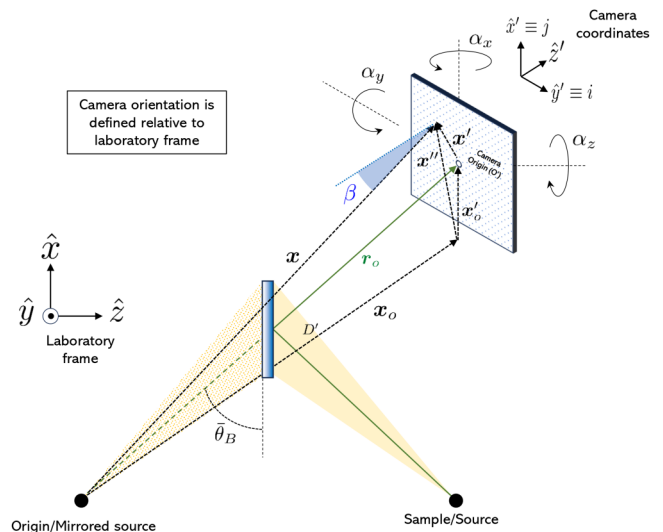
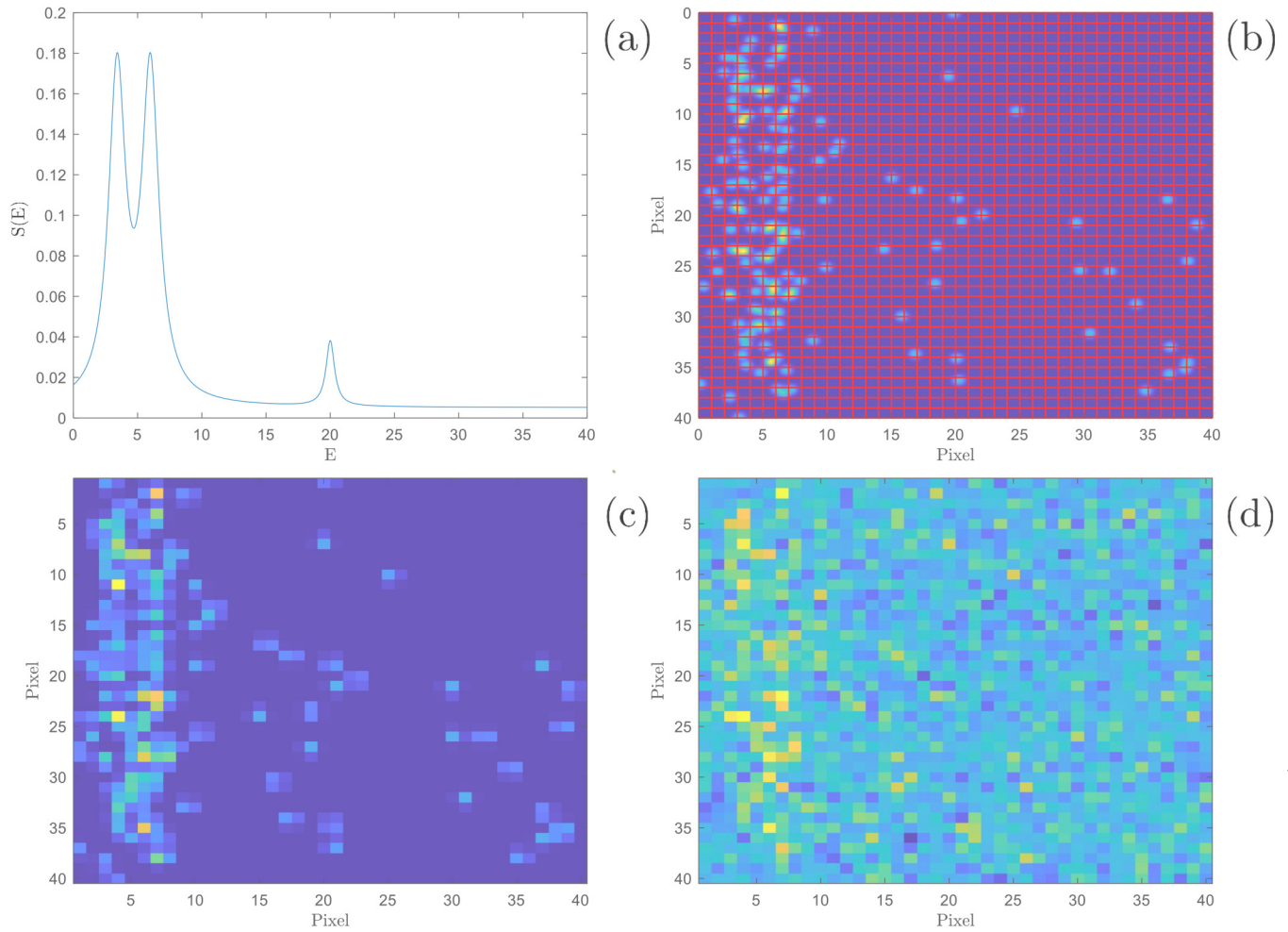


FIG. 10. Scheme for the solid angle calculations in the flat crystal spectrometer case.

10 April 2025 18:02:44



10 April 2025 18:02:44

FIG. 11. (a) The normalized spectrum used for producing the synthetic camera images. (b) The charge deposited on the camera surface, with the pixel grid depicted. (c) The ADU map on the pixel grid. (d) The final camera image with the noise applied.

$S(E_i)$ and the reconstructed spectrum $\tilde{S}(E_i)$. The latter is obtained by integrating the processed camera images along its columns and then normalizing it for comparison with $S(E_i)$. In Fig. 12, we compare, for $\lambda = 0.1$ and $\lambda = 1$, the original spectrum with the spectra reconstructed using different methods to treat the camera image. These methods include simple thresholding, only the photon counting algorithm, only the deconvolution algorithm, and the sequential application of photon counting and deconvolution techniques (“Hybrid” mode), as discussed in Sec. II D. Panel (a) shows that, for small λ values, the photon counting algorithm alone outperforms the deconvolution algorithm alone and the simple thresholding. This is because, in regions with very few photons—where ADU counts are mostly produced by noise—the photon counting algorithm achieves higher accuracy, outweighing the contributions from regions with a stronger signal. In contrast, for large λ values [panel (b)], the photon counting algorithm offers

little improvement over the thresholded image, whereas the deconvolution algorithm is able better to treat the regions with many photons, enhancing and better resolving the closely spaced spectral features (as seen in the two spectral lines at the lower end of the energy range). The sequential application of these two techniques (“Hybrid” mode) combines their benefits, yielding the best performances for both values of λ . We note that the applied method can have a substantial effect on the extracted spectral features, such as spectral linewidths or line ratios, which are often used as key diagnostics in experiments. For the RL deconvolution, we used the built-in Python function.⁷⁵ The number of iterations used in the RL algorithm was selected from a range of values by determining which provided the best match between the processed and original spectrum. The optimal value, found to be 100, was also applied to the analysis of experimental data, considering comparable levels of noise and charge spreading to the synthetic images.

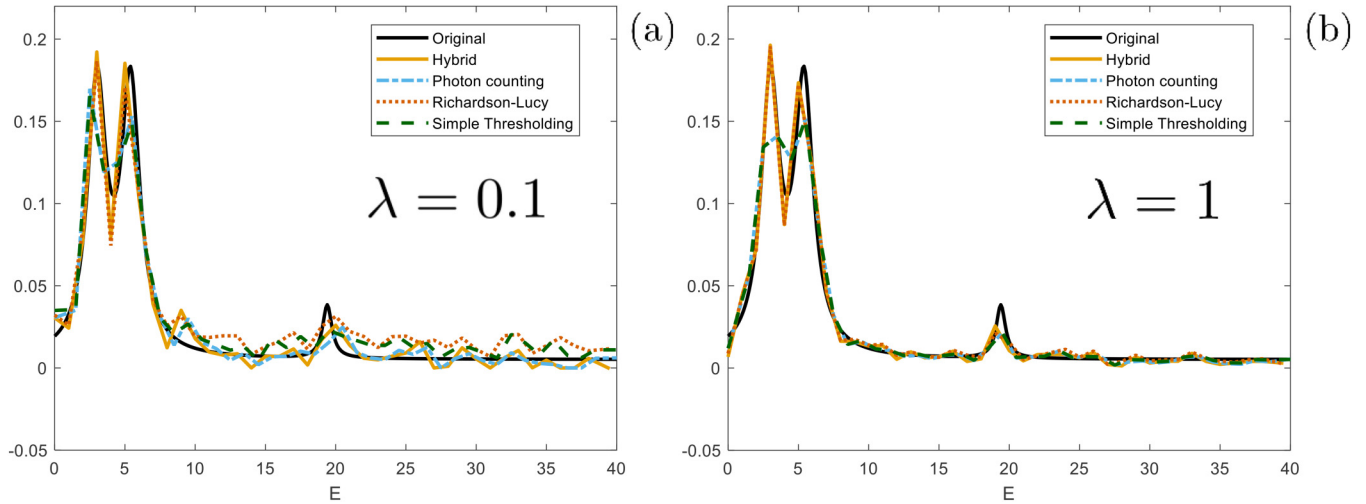


FIG. 12. The original spectrum compared, for $\lambda = 0.1$ (a) and $\lambda = 1$ (b), to the spectra reconstructed with different methods: Only the photon counting algorithm (“Photon counting”), only the deconvolution algorithm (“Richardson–Lucy”), both the techniques combined (“Hybrid”), and none of them (“Simple Thresholding”). The camera parameters are $R_s = 0.4$ and $\sigma_N = 30$.

To evaluate performance, we study the quality of the spectrum reconstructed from the “Hybrid”-processed image compared to that obtained by “Simple thresholding” of the raw image as a function of the filling fraction. The effect of changing the noise level is included in this study, as the ratio λ/σ_N is the dominant parameter determining the quality of the reconstruction. This analysis was conducted for two values of the charge spreading, $R_s = 0.3$ and $R_s = 0.6$ in pixel units, and its results are reported in Fig. 13. As anticipated, the “Hybrid”-processed image consistently yields a higher quality spectrum than the thresholded image across all λ values and for each R_s . The smallest difference occurs at intermediate λ values, where neither the photon counting algorithm nor the deconvolution algorithm is particularly effective. Additionally, the quality of the reconstruction improves for smaller R_s and larger λ , reaching an asymptote as $\lambda \rightarrow \infty$. This behavior is expected, as a larger number of photons on the camera reduces the Poissonian error and the relative strength of noise, while a smaller R_s facilitates the deconvolution process and the identification of the thresholding value, better separating the 0th and 1st peak in the histogram of photon counts.

B. Experimental data

In this section, we show the application of our analysis approach to a real camera image and the resulting improvements in the spectrum obtained. Figure 14 reports the MgF_2 emission spectrum introduced earlier, computed either with simple thresholding or with the image processing described in Sec. II D (“Hybrid” mode). The parameters used in these operations (ADU_{sp} , σ_N , λ) were determined by fitting a synthetic histogram to the experimental one [see Fig. 7(e)]. To generate the synthetic histogram, we used an estimated spectrum computed by integrating the camera signal over the energy contours defined by the energy map and the parameters

of the PIXIS-XF camera (the detector employed for this experiment), which were provided in the relevant documentation.⁷⁶ From this documentation and the fitting process, we obtained $R_s = 1.7$ in pixel unit, $ADU_{sp} = 43$ ADU and $\sigma_N = 4$ ADU, which were applied in the processing of the experimental images. For thresholding, we used the values specified in Sec. II D 1, expressed as a function of σ_N . The error bars for the two spectra were computed using

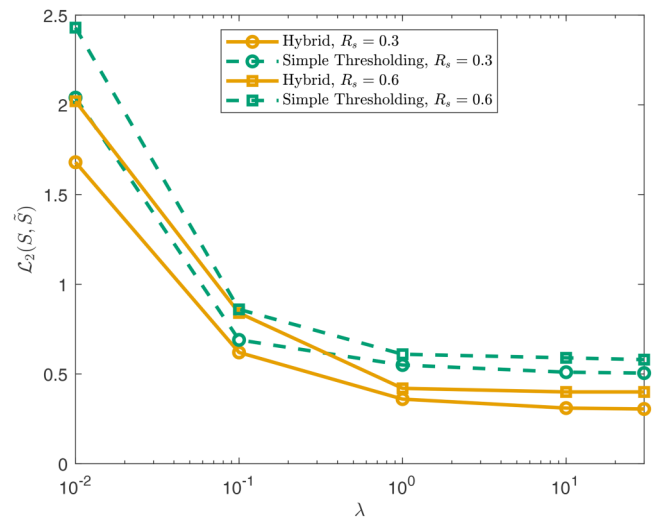


FIG. 13. \mathcal{L}_2 distance between the original spectrum and the one reconstructed from the processed and thresholded image as a function of the filling fraction, for two values of R_s . Note that the asymptote value is not zero, as discrepancies from charge spreading and finite pixel size persist in the limit $\lambda \rightarrow \infty$.

10 April 2025 18:02:44

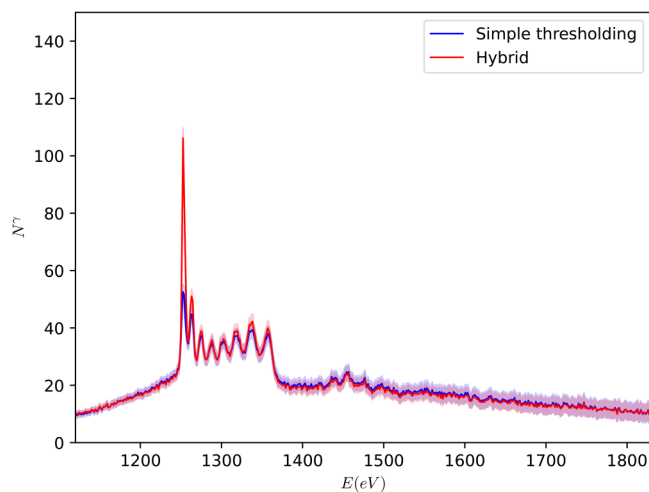


FIG. 14. Emission spectrum of MgF_2 obtained with simple thresholding (red) and processing the images with the photon counting and deconvolution methods (blue). Error bounds are indicated by shaded regions. The peaks in the spectrum correspond to the $K\alpha$ (from 1250 to 1370 eV) and $K\beta$ (from 1430 to 1500 eV) emission lines of the different ionization states of the Mg ions.

Poissonian inference and neglecting noise-related errors, drastically reduced by thresholding and integration over the energy contours. Details of these error calculations are provided in [Appendix C](#).

The enhancement of features is particularly noticeable for the narrowest and most intense ones, such as the low-energy peaks around 1260 eV. We believe that such improvements are mainly due to the reduction of the background noise, and they could, therefore, be essential when the physical information of the probed system is contained in weaker features (e.g., Raman scattering peaks). Moreover, the enhanced resolution achieved through the deconvolution algorithm for the narrowest and most intense peaks has significant implications for HED science, where line ratios and widths play a critical role. In this example, line ratios are essential for determining relative ion populations and, consequently, plasma temperature.⁷⁷ Temperature is also commonly inferred using x-ray Thomson scattering via detailed balance, where precise line ratio measurements are equally crucial.⁷⁸ On the other hand, accurate estimation of linewidths can be important for determining internal electromagnetic field intensities and collisional dynamic through Zeeman, Stark, and collisional broadening.^{79–82} For the photon counting algorithm to be effective, it must be applied to single-shot images rather than averaged ones, where single photon clusters are reduced by summation. This requirement, combined with the typical size of a camera image (here 2048×2048 pixels), makes the process time-consuming for real-time analysis. However, this procedure can be performed during post-analysis, where time constraints are less demanding. The current implementation takes approximately 8 min to process a single 2048×2048 image, which remains quite slow even for post-analysis. Improving the efficiency of these algorithms would greatly enhance their practical usability. Additionally, the computation can be parallelized by distributing

different regions of the image across multiple processors, significantly reducing processing time.

IV. CONCLUSIONS

In summary, we have provided a detailed guide for constructing spectra from the relative camera images for two of the most common geometries employed in x-ray spectroscopy. Specifically, we examined the computation of the energy map and the solid-angle correction for the pixel array, the estimation of important camera parameters such as the thermal noise intensity, and presented techniques to estimate the distribution of photon hits from the raw camera data, with the aim of increasing the SNR. These image processing techniques are based on the sequential combination of clustering algorithms and deconvolution methods for treating simultaneously regions with different local fill fractions. The application of these methods to both synthetic and experimental data demonstrated notable improvements in SNR and feature clarity, demonstrating their importance in contexts where the measured physical features are weak and the precise determination of linewidths and intensities is crucial. Future work could explore enhancing the capacity for multi-photon cluster identification, including expanding the variety of allowed cluster shapes. Additionally, it would be useful to integrate this work with studies on the instrument function and combine the improvement to the SNR demonstrated here with an access to enhanced resolution.

ACKNOWLEDGMENTS

A.F. and S.M.V. acknowledge support for the STFC UK Hub for the Physical Sciences on XFELS. T.G. and S.M.V. acknowledge support from AWE via the Oxford Centre for High Energy Density Science (OxCHEDS). T.C. and S.M.V. acknowledge support from the Royal Society. Y.S. and S.M.V. acknowledge support from the UK EPSRC under Grant Nos. EP/P015794/1 and EP/W010097/1. T.G. acknowledges support by the Center for Advanced Systems Understanding (CASUS), financed by Germany's Federal Ministry of Education and Research (BMBF) and the Saxon state government out of the state budget approved by the Saxon State Parliament. This work has received funding from the European Union's Just Transition Fund (JTF) within the project Röntgenlaser-Optimierung der Laserfusion (ROLF), Contract No. 5086999001, co-financed by the Saxon state government out of the state budget approved by the Saxon State Parliament.

AUTHOR DECLARATIONS

Conflict of Interest

The authors have no conflicts to disclose.

Author Contributions

A.F., O.S.H., T.G., and S.M.V. developed the methods. A.F. and T.G. implemented the codes, with contributions from O.S.H., T.C., and Y.S. A.F. wrote the manuscript with contributions from T.G. and O.S.H., and all authors reviewed and edited the final version. S.M.V. supervised the project.

10 April 2025 18:02:44

Alessandro Forte: Conceptualization (equal); Data curation (equal); Formal analysis (lead); Investigation (lead); Methodology (equal); Software (equal); Validation (lead); Writing – original draft (lead). **Thomas Gawne:** Conceptualization (equal); Data curation (supporting); Formal analysis (supporting); Funding acquisition (lead); Methodology (supporting); Project administration (lead); Resources (lead); Software (equal); Supervision (lead); Validation (supporting); Writing – original draft (supporting); Writing – review & editing (equal). **Oliver S. Humphries:** Conceptualization (equal); Data curation (supporting); Formal analysis (equal); Methodology (equal); Software (equal); Validation (supporting); Writing – original draft (supporting); Writing – review & editing (equal). **Thomas Campbell:** Conceptualization (supporting); Methodology (supporting); Software (supporting); Writing – review & editing (supporting). **Yuanfeng Shi:** Conceptualization (supporting); Data curation (supporting); Formal analysis (equal); Methodology (supporting); Validation (supporting); Writing – review & editing (supporting). **Sam M. Vinko:** Conceptualization (equal); Funding acquisition (lead); Methodology (equal); Project administration (lead); Resources (lead); Supervision (lead); Validation (supporting); Writing – review & editing (equal).

DATA AVAILABILITY

The data that support the findings of this study are available from the corresponding author upon reasonable request.

APPENDIX A: DETERMINATION OF THRESHOLDING VALUES

The two thresholding values can be determined using the following procedure. First, we generate N_s synthetic images (see also Sec. III A) for specified parameters (ADU_{sp} , σ_N , R_s) and for a small fill fraction (e.g., $\lambda = 0.1$) so that single-photon clusters are predominant. Each of these synthetic images is then processed with the photon clustering algorithm, applying a trial pair of thresholding values, and divided by ADU_{sp} to reconstruct the photon hits map $\{N^{rec}\}$. The reconstructed photon maps are then compared to the original photon map $\{N^{orig}\}$, and a global loss function is computed,

$$\mathcal{L}_{oss} = \frac{1}{N_s} \sum_{l=1}^{N_s} \mathcal{L}_F(\{N^{rec}\}_l - \{N^{orig}\}), \quad (\text{A1})$$

where $\{N^{rec}\}_l$ and $\{N^{orig}\}$ are two matrices and \mathcal{L}_F is the Frobenius norm. The optimal threshold pair is obtained as the one that minimizes this loss function.

APPENDIX B: PROBABILITY DISTRIBUTION OF THE ADU COUNTS

Let us focus on regions with high local λ , where the photon counting algorithm leaves pixel values unchanged. While this discussion can be extended to include thresholding and charge accumulation operations, doing so adds complexity without altering the fundamental concepts. First, consider the signal on a sufficiently

fine subgrid $k, l = 1, 2, \dots$ (see also Sec. III A),

$$A_{kl} = \sum_{k'l'} ADU_{sp} (N_{k'l'}^\gamma + \beta_{k'l'}) H_{k-k' \ l-l'}, \quad (\text{B1})$$

where H is the charge spreading function and $N_{k'l'}^\gamma \sim \text{Poisson}(I_{k'l'})$, with $I_{k'l'}$ denoting the spectral intensity at subpixel $(k'l')$. The term $\beta_{k'l'} \sim \mathcal{N}(0, fN_{k'l'}^\gamma)$ is a compound probability distribution accounting for random fluctuations in e–h pairs production, quantified by the Fano factor f . This factor is usually small (e.g., $f = 0.12$ in Silicon⁵¹), and therefore, this noise source is often neglected. The value A_{ij} is obtained by summing A_{kl} over the subpixels within each pixel and then adding the thermal noise specific to the pixel,

$$A_{ij} = \sum_{k,l \in (i,j)} A_{kl} + \eta_{ij}, \quad (\text{B2})$$

where $k, l \in (i, j)$ indicates that subpixel (k, l) lies in pixel (i, j) . Using the properties of the Poisson distribution and neglecting the e–h pairs production noise, we can now write

$$\begin{aligned} A_{ij} &= \sum_{k,l \in (i,j)} \sum_{k'l'} ADU_{sp} \text{Poisson}(I_{k'l'}) H_{k-k' \ l-l'} + \eta_{ij} \\ &= ADU_{sp} \text{Poisson} \left(\sum_{k,l \in (i,j)} \sum_{k'l'} I_{k'l'} H_{k-k' \ l-l'} \right) + \eta_{ij} \\ &= ADU_{sp} \text{Poisson} \left(\sum_{i'j'} \sum_{k'l' \in (i',j')} I_{k'l'} \sum_{k,l \in (i,j)} H_{k-k' \ l-l'} \right) + \eta_{ij} \\ &\approx ADU_{sp} \text{Poisson} \left(\sum_{i'j'} \bar{I}_{i'j'} \sum_{k'l' \in (i',j')} \sum_{k,l \in (i,j)} H_{k-k' \ l-l'} \right) + \eta_{ij} \\ &= ADU_{sp} \text{Poisson} \left(\sum_{i'j'} I_{i'j'} \tilde{H}_{i-i' \ j-j'} \right) + \eta_{ij} \\ &= ADU_{sp} \sum_{i'j'} \text{Poisson}(I_{i'j'}) \tilde{H}_{i-i' \ j-j'} + \eta_{ij}, \end{aligned} \quad (\text{B3})$$

where we reasonably assumed $I_{k'l'}$ to be constant within each pixel and equal to $\bar{I}_{i'j'}$. Here, we defined $I_{i'j'} = \sum_{k'l' \in (i',j')} I_{k'l'} \approx N_p \bar{I}_{i'j'}$, with N_p representing the number of subpixels per pixel, and an effective charge spreading function as

$$\tilde{H}_{i-i' \ j-j'} = \frac{1}{N_p} \sum_{i'k' \in (i',j')} \sum_{ik \in (i,j)} H_{k-k' \ l-l'}. \quad (\text{B4})$$

The translation invariance of \tilde{H} follows directly from the inherent translation invariance of H . Equation (B3) proves that the operation defined by Eq. (20), combined with the division in Eq. (21), yields an estimate for I_{ij} .

APPENDIX C: ERROR CALCULATIONS

We begin by computing the best estimate of the parameter I (also the mean) of a Poisson distribution, given an observation n ,

$$N \sim \text{Poisson}(I) \Rightarrow \mathcal{P}(N = n|I) = \frac{I^n e^{-I}}{n!}. \quad (\text{C1})$$

Assuming a flat prior distribution for I over a large interval $[0, M]$ (since I cannot be infinitely large), and noting that $\mathcal{P}(n) = \int_0^M \mathcal{P}(n|I)\mathcal{P}(I) dI = \int_0^M dI \frac{I^n e^{-I}}{n!} \approx \frac{1}{M}$ if M is sufficiently large, from Bayes' theorem, we find

$$\mathcal{P}(I|n) = \frac{\mathcal{P}(n|I)\mathcal{P}(I)}{\mathcal{P}(n)} = \mathcal{P}(n|I). \quad (\text{C2})$$

From this equation, we can calculate the best estimate for I as

$$\langle I \rangle(n) = \int_0^M dI I \mathcal{P}(I|n) = \int_0^M dI I \frac{I^n e^{-I}}{n!} \approx n + 1. \quad (\text{C3})$$

Similarly, we determine the error on this estimate as the standard deviation of $\mathcal{P}(I|n)$,

$$\sqrt{\langle I^2 \rangle - \langle I \rangle^2}(n) \approx \sqrt{n + 1}. \quad (\text{C4})$$

To analyze our case, we consider $\tilde{I}(E_i) = \sum_{ij|E_{ij} \in \Delta E_i} N_{ij}^{\gamma}$ as a realization of the random variable $I(E_i) \sim \text{Poisson}(\Omega(E_i)S(E_i))$. Here, we are disregarding the contribution to $I(E_i)$ from noise, which is generally small due to the thresholding operations and the summation over many pixels. Additionally, we are not considering the error propagation through processing steps, taking instead directly N_{ij}^{γ} as the estimate of the photon hits map. Under these assumptions, the spectrum and its error, for each energy bin, are given by

$$\langle S(E_i) \rangle = \frac{\tilde{I}(E_i) + 1}{\Omega(E_i)} \quad \sigma(S(E_i)) = \frac{\sqrt{\tilde{I}(E_i) + 1}}{\Omega(E_i)}. \quad (\text{C5})$$

As a final consideration, we observe that the error normalized to the signal, $\sigma(S(E_i))/\langle S(E_i) \rangle = 1/\sqrt{\tilde{I}(E_i) + 1}$, correctly decreases as the number of photons per bin increases.

REFERENCES

- ¹M. Born and E. Wolf, *Principles of Optics: Electromagnetic Theory of Propagation, Interference and Diffraction of Light* (Elsevier, 2013).
- ²R. Foord, R. Jones, C. Oliver, and E. Pike, "The use of photomultiplier tubes for photon counting," *Appl. Opt.* **8**, 1975 (1969).
- ³P. Alle, E. Wenger, S. Dohaoui, D. Schaniel, and C. Lecomte, "Comparison of CCD, CMOS, and hybrid pixel X-ray detectors: Detection principle and data quality," *Phys. Script.* **91**(6), 063001 (2016).
- ⁴S. Svanberg, *Atomic and Molecular Spectroscopy: Basic Aspects and Practical Applications* (Springer Science & Business Media, 2012), Vol. 6.
- ⁵P. Schmüser, M. Dohlus, J. Rossbach, and C. Behrens, *Free-Electron Lasers in the Ultraviolet and X-Ray Regime*, Springer Tracts in Modern Physics (Springer, 2014), Vol. 258.
- ⁶D. Jaroszynski, R. Bingham, E. Brunetti, B. Ersfeld, J. Gallacher, B. van Der Geer, R. Issac, S. Jamison, D. Jones, M. De Loos *et al.*, "Radiation sources based on laser-plasma interactions," *Philos. Trans. R. Soc. A Math. Phys. Eng. Sci.* **364**, 689 (2006).
- ⁷M. G. Haines, "A review of the dense Z-pinch," *Plasma Phys. Contr. Fus.* **53**(9), 093001 (2011).
- ⁸P. L. Franz, Z. Guo, D. Bohler, D. Cesar, X. Cheng, T. Driver, J. Duris, A. Kamalov, S. Li, M.-F. Lin, R. Obaid, R. Robles, N. Sudar, A. L. Wang, Z. Zhang, J. P. Cryan, and A. Marinelli, "Development of attosecond capabilities at LCLS," in *The International Conference on Ultrafast Phenomena (UP) 2022* (Optica Publishing Group, 2022).
- ⁹J. Amann, W. Berg, V. Blank, F.-J. Decker, Y. Ding, P. Emma, Y. Feng, J. Frisch, D. Fritz, J. Hastings *et al.*, "Demonstration of self-seeding in a hard-x-ray free-electron laser," *Nat. Photonics* **6**, 693 (2012).
- ¹⁰J. Yamada, S. Matsuyama, I. Inoue, T. Osaka, T. Inoue, N. Nakamura, Y. Tanaka, Y. Inubushi, T. Yabuuchi, K. Tono *et al.*, "Extreme focusing of hard X-ray free-electron laser pulses enables 7 nm focus width and 1022 W cm⁻² intensity," *Nat. Photonics* **18**, 685 (2024).
- ¹¹T. M. Jeong and J. Lee, "Femtosecond petawatt laser," *Ann. Phys.* **526**, 157 (2014).
- ¹²D. Papadopoulos, J. Zou, C. Le Blanc, G. Chériaux, P. Georges, F. Druon, G. Mennerat, P. Ramirez, L. Martin, A. Frénaux *et al.*, "The apollon 10 PW laser: Experimental and theoretical investigation of the temporal characteristics," *High Power Laser Sci. Eng.* **4**, e34 (2016).
- ¹³G. H. Miller, E. I. Moses, and C. R. Wuest, "The national ignition facility," *Opt. Eng.* **43**, 2841 (2004).
- ¹⁴J. Eggert, D. Hicks, P. Celliers, D. Bradley, R. McWilliams, R. Jeanloz, J. Miller, T. Boehly, and G. Collins, "Melting temperature of diamond at ultrahigh pressure," *Nat. Phys.* **6**, 40 (2010).
- ¹⁵A. B. Zylstra, O. A. Hurricane, D. A. Callahan, A. L. Kritcher, J. E. Ralph, H. F. Robey, J. S. Ross, C. V. Young, K. L. Baker, D. T. Casey *et al.*, "Burning plasma achieved in inertial fusion," *Nature* **601**, 542 (2022).
- ¹⁶H. Abu-Shawareb, R. Acree, P. Adams, J. Adams, B. Addis, R. Aden, P. Adrian, B. B. Afeyan, M. Aggleton, L. Aghaian *et al.* and Indirect Drive ICF Collaboration, "Lawson criterion for ignition exceeded in an inertial fusion experiment," *Phys. Rev. Lett.* **129**, 075001 (2022).
- ¹⁷H. Abu-Shawareb, R. Acree, P. Adams, J. Adams, B. Addis, R. Aden, P. Adrian, B. B. Afeyan, M. Aggleton, L. Aghaian *et al.* and The Indirect Drive ICF Collaboration, "Achievement of target gain larger than unity in an inertial fusion experiment," *Phys. Rev. Lett.* **132**, 065102 (2024).
- ¹⁸D. Kraus, A. Ravasio, M. Gauthier, D. O. Gericke, J. Vorberger, S. Frydrych, J. Helfrich, L. B. Fletcher, G. Schaumann, B. Nagler, B. Barbel, B. Bachmann, E. J. Gamboa, S. Göde, E. Granados, G. Gregori, H. J. Lee, P. Neumayer, W. Schumaker, T. Döppner, R. W. Falcone, S. H. Glenzer, and M. Roth, "Nanosecond formation of diamond and lonsdaleite by shock compression of graphite," *Nat. Commun.* **7**, 10970 (2016).
- ¹⁹M. Miao, Y. Sun, E. Zurek, and H. Lin, "Chemistry under high pressure," *Nat. Rev. Chem.* **4**, 508 (2020).
- ²⁰S. Toleikis, T. Bornath, T. Döppner, S. Düsterer, R. R. Fäustlin, E. Förster, C. Fortmann, S. H. Glenzer, S. Göde, G. Gregori, R. Irsig, T. Laarmann, H. J. Lee, B. Li, K.-H. Meiwe-Broer, J. Mithen, B. Nagler, A. Przystawik, P. Radcliffe, H. Redlin, R. Redmer, H. Reinholz, G. Röpke, F. Tavella, R. Thiele, J. Tiggesbäumker, I. Uschmann, S. M. Vinko, T. Whitcher, U. Zastrau, B. Ziaja, and T. Tschentscher, "Probing near-solid density plasmas using soft x-ray scattering," *J. Phys. B: At., Mol. Opt. Phys.* **43**, 194017 (2010).
- ²¹L. B. Fletcher, H. J. Lee, T. Döppner, E. Galtier, B. Nagler, P. Heimann, C. Fortmann, S. LePape, T. Ma, M. Millot, A. Pak, D. Turnbull, D. A. Chapman, D. O. Gericke, J. Vorberger, T. White, G. Gregori, M. Wei, B. Barbel, R. W. Falcone, C. C. Kao, H. Nuhn, J. Welch, U. Zastrau, P. Neumayer, J. B. Hastings, and S. H. Glenzer, "Ultrabright X-ray laser scattering for dynamic warm dense matter physics," *Nat. Photonics* **9**, 274 (2015).
- ²²O. Ciricosta, S. M. Vinko, H.-K. Chung, B.-I. Cho, C. R. D. Brown, T. Burian, J. Chalupský, K. Engelhorn, R. W. Falcone, C. Graves, V. Hájková,

- A. Higginbotham, L. Juha, J. Krzywinski, H. J. Lee, M. Messerschmidt, C. D. Murphy, Y. Ping, D. S. Rackstraw, A. Scherz, W. Schlotter, S. Toleikis, J. J. Turner, L. Vysin, T. Wang, B. Wu, U. Zastra, D. Zhu, R. W. Lee, P. Heimann, B. Nagler, and J. S. Wark, "Direct measurements of the ionization potential depression in a dense plasma," *Phys. Rev. Lett.* **109**, 065002 (2012).
- ²³T. Gawne, T. Campbell, A. Forte, P. Hollebon, G. Perez-Callejo, O. S. Humphries, O. Karnbach, M. F. Kasim, T. R. Preston, H. J. Lee, A. Miscampbell, Q. Y. van den Berg, B. Nagler, S. Ren, R. B. Royle, J. S. Wark, and S. M. Vinko, "Investigating mechanisms of state localization in highly ionized dense plasmas," *Phys. Rev. E* **108**, 035210 (2023).
- ²⁴P. Hollebon, O. Ciricosta, M. P. Desjarlais, C. Cacho, C. Spindloe, E. Springate, I. C. E. Turcu, J. S. Wark, and S. M. Vinko, "Ab initio simulations and measurements of the free-free opacity in aluminum," *Phys. Rev. E* **100**, 043207 (2019).
- ²⁵T. R. Preston, S. M. Vinko, O. Ciricosta, P. Hollebon, H.-K. Chung, G. L. Dakovski, J. Krzywinski, M. Minitti, T. Burian, J. Chalupsky, V. Hájková, L. Juha, V. Vozda, U. Zastra, R. W. Lee, and J. S. Wark, "Measurements of the K-shell opacity of a solid-density magnesium plasma heated by an X-ray free-electron laser," *Phys. Rev. Lett.* **119**, 085001 (2017).
- ²⁶S. M. Vinko, V. Vozda, J. Andreasson, S. Bajt, J. Bielecki, T. Burian, J. Chalupsky, O. Ciricosta, M. P. Desjarlais, H. Fleckenstein, J. Hajdu, V. Hájková, P. Hollebon, L. Juha, M. F. Kasim, E. E. McBride, K. Muehlig, T. R. Preston, D. S. Rackstraw, S. Roling, S. Toleikis, J. S. Wark, and H. Zacharias, "Time-resolved XUV opacity measurements of warm dense aluminum," *Phys. Rev. Lett.* **124**, 225002 (2020).
- ²⁷S. M. Vinko, O. Ciricosta, T. R. Preston, D. S. Rackstraw, C. R. D. Brown, T. Burian, J. Chalupsky, B. I. Cho, H. K. Chung, K. Engelhorn, R. W. Falcone, R. Fiokovini, V. Hájková, P. A. Heimann, L. Juha, H. J. Lee, R. W. Lee, M. Messerschmidt, B. Nagler, W. Schlotter, J. J. Turner, L. Vysin, U. Zastra, and J. S. Wark, "Investigation of femtosecond collisional ionization rates in a solid-density aluminium plasma," *Nat. Commun.* **6**, 6397 (2015).
- ²⁸Q. Y. van den Berg, E. V. Fernandez-Tello, T. Burian, J. Chalupsky, H.-K. Chung, O. Ciricosta, G. L. Dakovski, V. Hájková, P. Hollebon, L. Juha, J. Krzywinski, R. W. Lee, M. P. Minitti, T. R. Preston, A. G. de la Varga, V. Vozda, U. Zastra, J. S. Wark, P. Velarde, and S. M. Vinko, "Clocking femtosecond collisional dynamics via resonant x-ray spectroscopy," *Phys. Rev. Lett.* **120**, 055002 (2018).
- ²⁹P. Willmott, *An Introduction to Synchrotron Radiation: Techniques and Applications* (John Wiley & Sons, 2019).
- ³⁰S. Vinko, O. Ciricosta, B. Cho, K. Engelhorn, H.-K. Chung, C. Brown, T. Burian, J. Chalupsky, R. Falcone, C. Graves *et al.*, "Creation and diagnosis of a solid-density plasma with an X-ray free-electron laser," *Nature* **482**, 59 (2012).
- ³¹D. Milathianaki, S. Boutet, G. J. Williams, A. Higginbotham, D. Ratner, A. E. Gleason, M. Messerschmidt, M. M. Seibert, D. C. Swift, P. Hering, J. Robinson, W. E. White, and J. S. Wark, "Femtosecond visualization of lattice dynamics in shock-compressed matter," *Science* **342**, 220 (2013).
- ³²C. E. Wehrenberg, D. McGonegle, C. Bolme, A. Higginbotham, A. Lazicki, H. J. Lee, B. Nagler, H. S. Park, B. A. Remington, R. E. Rudd, M. Sliwa, M. Suggit, D. Swift, F. Tavella, L. Zepeda-Ruiz, and J. S. Wark, "In situ X-ray diffraction measurement of shock-wave-driven twinning and lattice dynamics," *Nature* **550**, 496 (2017).
- ³³O. Müller, D. Lützenkirchen-Hecht, and R. Frahm, "Quick scanning monochromator for millisecond in situ and in operando x-ray absorption spectroscopy," *Rev. Sci. Instrum.* **86**, 093905 (2015).
- ³⁴A. G. Basden, C. Haniff, and C. Mackay, "Photon counting strategies with low-light-level CCDs," *Mon. Not. R. Astron. Soc.* **345**, 985 (2003).
- ³⁵C. H. Lewenkopf, E. R. Mucciolo, and A. Castro Neto, "Numerical studies of conductivity and fano factor in disordered graphene," *Phys. Rev. B* **77**, 081410 (2008).
- ³⁶R. C. Jone, "Quantum efficiency of detectors for visible and infrared radiation," *Adv. Electron. Electron Phys.* **11**, 87 (1959).
- ³⁷M. V. Newberry, "Signal-to-noise considerations for sky-subtracted CCD data," *Publ. Astron. Soc. Pac.* **103**, 122 (1991).
- ³⁸H. Du and K. J. Voss, "Effects of point-spread function on calibration and radiometric accuracy of CCD camera," *Appl. Opt.* **43**, 665 (2004).
- ³⁹A. Abboud, S. Send, N. Pashniak, W. Leitenberger, S. Ihle, M. Huth, R. Hartmann, L. Strüder, and U. Pietsch, "Sub-pixel resolution of a pnCCD for X-ray white beam applications," *J. Instrum.* **8**(05), P05005 (2013).
- ⁴⁰K. Hagino, K. Oono, K. Negishi, K. Yarita, T. Kohmura, T. G. Tsuru, T. Tanaka, H. Uchida, S. Harada, T. Okuno *et al.*, "Measurement of charge cloud size in X-ray SOI pixel sensors," *IEEE Trans. Nucl. Sci.* **66**, 1897 (2019).
- ⁴¹E. Gatti, A. Longoni, P. Rehak, and M. Sampietro, "Dynamics of electrons in drift detectors," *Nucl. Instrum. Methods Phys. Res. Sect. A* **253**, 393 (1987).
- ⁴²J. R. Janesick, K. P. Klaasen, and T. Elliott, "Charge-coupled-device charge-collection efficiency and the photon-transfer technique," *Opt. Eng.* **26**, 972 (1987).
- ⁴³P. M. Epperson, J. V. Sweedler, R. B. Billhorn, G. R. Sims, and M. B. Denton, "Applications of charge transfer devices in spectroscopy," *Anal. Chem.* **60**, 327A (1988).
- ⁴⁴B. P. Lathi and Z. Ding, *Modern Digital and Analog Communication Systems* (Oxford University Press, New York, 1998), Vol. 3.
- ⁴⁵J. C. Mullikin, L. J. van Vliet, H. Netten, F. R. Boddeke, G. Van der Feltz, and I. T. Young, "Methods for CCD camera characterization," in *Image Acquisition and Scientific Imaging Systems* (SPIE, 1994), Vol. 2173, pp. 73–84.
- ⁴⁶A. Shor, Y. Eisen, and I. Mardor, "Edge effects in pixelated CdZnTe gamma detectors," *IEEE Trans. Nucl. Sci.* **51**, 2412 (2004).
- ⁴⁷G. Morton, "Photon counting," *Appl. Opt.* **7**, 1 (1968).
- ⁴⁸E. Gamboa, B. Bachmann, D. Kraus, M. MacDonald, M. Bucher, S. Carron, R. Coffee, R. Drake, J. Emig, K. Ferguson *et al.*, "Dual crystal x-ray spectrometer at 1.8 keV for high repetition-rate single-photon counting spectroscopy experiments," *J. Instrum.* **11**(08), P08015 (2016).
- ⁴⁹W. Zachariasen, "A general theory of x-ray diffraction in crystals," *Acta Crystallogr.* **23**, 558 (1967).
- ⁵⁰O. Humphries, "Isochoric generation and spectroscopic diagnosis of high energy-density systems," Ph.D. thesis (University of Oxford, 2020).
- ⁵¹H. Goldstein, *Classical Mechanics* (Addison-Wesley, 1980).
- ⁵²F. Gao and L. Han, "Implementing the nelder-mead simplex algorithm with adaptive parameters," *Comput. Optim. Appl.* **51**, 259 (2012).
- ⁵³L. V. Hámos, "Röntgenspektroskopie und Abbildung mittels gekrümmter kristallreflektoren," *Naturwissenschaften* **20**, 705 (1932).
- ⁵⁴A. Forte, T. Gawne, K. K. Alaa El-Din, O. S. Humphries, T. R. Preston, C. Crépinsson, T. Campbell, P. Svensson, S. Azadi, P. Heighway *et al.*, "Resonant inelastic x-ray scattering in warm-dense Fe compounds beyond the SASE FEL resolution limit," *Commun. Phys.* **7**, 266 (2024).
- ⁵⁵D. Taupin, "Théorie dynamique de la diffraction des rayons x par les cristaux déformés," *Bulletin de Minéralogie* **87**, 469 (1964).
- ⁵⁶I. Uschmann, E. Förster, K. Gäbel, G. Hölzer, and M. Ensslen, "X-ray reflection properties of elastically bent perfect crystals in bragg geometry," *J. Appl. Crystallogr.* **26**, 405 (1993).
- ⁵⁷T. Gawne, H. Bellenbaum, L. B. Fletcher, K. Appel, C. Baecht, V. Bouffettier, E. Brambrink, D. Brown, A. Cangi, A. Descamps, S. Göde, N. J. Hartley, M.-L. Herbert, P. Hesselbach, H. Höppner, O. S. Humphries, Z. Konôpková, A. Laso, B. Lindqvist, J. Lütger, M. J. MacDonald, M. Makita, W. Martin, M. Mishchenko, Z. A. Moldabekov, M. Nakatsutsumi, J.-P. Naedler, P. Neumayer, A. Pelka, C. Qu, L. Randolph, J. Rips, T. Toncian, J. Vorberger, L. Wollenweber, U. Zastra, D. Kraus, T. R. Preston, and T. Dornheim, "Effects of mosaic crystal instrument functions on x-ray Thomson scattering diagnostics," *arXiv:2406.03301* [physics.plasm-ph] (2024).
- ⁵⁸T. Preston *et al.*, "Design and performance characterisation of the HAPG von Hámos spectrometer at the high energy density instrument of the european XFEL," *J. Instrum.* **15**, P11033 (2020).
- ⁵⁹U. Zastra, C. R. D. Brown, T. Döppner, S. H. Glenzer, G. Gregori, H. J. Lee, H. Marschner, S. Toleikis, O. Wehrhan, and E. Förster, "Focal aberrations of large-aperture HOPG von-Hámos x-ray spectrometers," *J. Instrum.* **7**(09), P09015 (2012).
- ⁶⁰U. Zastra, A. Woldegeorgis, E. Förster, R. Loetzsch, H. Marschner, and I. Uschmann, "Characterization of strongly-bent HAPG crystals for von-Hámos x-ray spectrographs," *J. Instrum.* **8**(10), P10006 (2013).
- ⁶¹S. Glenzer, L. Fletcher, E. Galtier, B. Nagler, R. Alonso-Mori, B. Barbrel, S. Brown, D. Chapman, Z. Chen, C. Curry *et al.*, "Matter under extreme

conditions experiments at the linac coherent light source,” *J. Phys. B: At. Mol. Opt. Phys.* **49**, 092001 (2016).

⁶²M. MacDonald, A. Saunders, B. Bachmann, M. Bethkenhagen, L. Divol, M. Doyle, L. Fletcher, S. Glenzer, D. Kraus, O. Landen *et al.*, “Demonstration of a laser-driven,” *Phys. Plasmas* **28**, 084303 (2021).

⁶³A. Mozzanica, M. Andrä, R. Barten, A. Bergamaschi, S. Chirioti, M. Brückner, R. Dinapoli, E. Fröjd, D. Greiffenberg, F. Leonarski *et al.*, “The jungfrau detector for applications at synchrotron light sources and XFELS,” *Synchrotron Radiat. News* **31**, 16 (2018).

⁶⁴J. Chalupský, J. Krzywinski, L. Juha, V. Hájková, J. Cihelka, T. Burian, L. Vyšín, J. Gaudin, A. Gleeson, M. Jurek, A. R. Khorsand, D. Klinger, H. Wabnitz, R. Sobierajski, M. Störmer, K. Tiedtke, and S. Toleikis, “Spot size characterization of focused non-Gaussian X-ray laser beams,” *Opt. Express* **18**, 27836 (2010).

⁶⁵C. Schlesiger, L. Anklamm, W. Malzer, R. Gnewkow, and B. Kanngießer, “A new model for the description of X-ray diffraction from mosaic crystals for ray-tracing calculations,” *J. Appl. Crystallogr.* **50**, 1490 (2017).

⁶⁶W. Dusi, N. Auricchio, L. Brigliadori, A. Donati, G. Landini, D. Mengoni, E. Perillo, and G. Ventura, “A study of the spectroscopic response of planar CdTe detectors when irradiated at various angles of incidence,” *Nucl. Instrum. Methods Phys. Res. Sect. A* **506**, 119 (2003).

⁶⁷M. Gerlach, L. Anklamm, A. Antonov, I. Grigorieva, I. Holfelder, B. Kanngießer, H. Legall, W. Malzer, C. Schlesiger, and B. Beckhoff, “Characterization of HAPG mosaic crystals using synchrotron radiation,” *J. Appl. Crystallogr.* **48**, 1381 (2015).

⁶⁸J. Feldhaus, E. Saldin, J. Schneider, E. Schneidmiller, and M. Yurkov, “Possible application of x-ray optical elements for reducing the spectral bandwidth of an x-ray sase fel,” *Opt. Commun.* **140**, 341 (1997).

⁶⁹L. Wollenweber, T. Preston, A. Descamps, V. Cerantola, A. Comley, J. Eggert, L. Fletcher, G. Geloni, D. Gericke, S. Glenzer *et al.*, “High-resolution inelastic x-ray scattering at the high energy density scientific instrument at the european x-ray free-electron laser,” *Rev. Sci. Instrum.* **92**, 1231 (2021).

⁷⁰E. E. McBride, T. White, A. Descamps, L. Fletcher, K. Appel, F. Condamine, C. Curry, F. Dallari, S. Funk, E. Galtier *et al.*, “Setup for meV-resolution inelastic X-ray scattering measurements and X-ray diffraction at the matter in extreme conditions endstation at the linac coherent light source,” *Rev. Sci. Instrum.* **89**, 129901 (2018).

⁷¹K. Voigt, M. Zhang, K. Ramakrishna, A. Amouretti, K. Appel, E. Brambrink, V. Cerantola, D. Chekrygina, T. Döppner, R. W. Falcone, K. Falk, L. B. Fletcher,

D. O. Gericke, S. Góde, M. Harmand, N. J. Hartley, S. P. Hau-Riege, L. G. Huang, O. S. Humphries, M. Lokamani, M. Makita, A. Pelka, C. Prescher, A. K. Schuster, M. Šmíd, T. Toncian, J. Vorberger, U. Zastra, T. R. Preston, and D. Kraus, “Demonstration of an x-ray Raman spectroscopy setup to study warm dense carbon at the high energy density instrument of European XFEL,” *Phys. Plasmas* **28**, 082701 (2021).

⁷²G. Hölzer, M. Fritsch, M. Deutsch, J. Härtwig, and E. Förster, “ $k\alpha_{1,2}$ and $k\beta_{1,3}$ x-ray emission lines of the 3d transition metals,” *Phys. Rev. A* **56**, 4554 (1997).

⁷³G. Carini, R. Alonso-Mori, G. Blaj, P. Caragiulo, M. Chollet, D. Damiani, A. Dragone, Y. Feng, G. Haller, P. Hart *et al.*, “ePix100 camera: Use and applications at LCLS,” in *AIP Conference Proceedings* (AIP Publishing, 2016), Vol. 1741.

⁷⁴W. H. Richardson, “Bayesian-based iterative method of image restoration,” *JoSA* **62**, 55 (1972).

⁷⁵scikit image, skimage.restoration library.

⁷⁶M. Yaffe and J. Rowlands, “X-ray detectors for digital radiography,” *Phys. Med. Biol.* **42**, 1 (1997).

⁷⁷O. Ciricosta, S. Vinko, H.-K. Chung, C. Jackson, R. Lee, T. Preston, D. Rackstraw, and J. Wark, “Detailed model for hot-dense aluminum plasmas generated by an x-ray free electron laser,” *Phys. Plasmas* **23**, 022707 (2016).

⁷⁸T. Döppner, O. Landen, H. Lee, P. Neumayer, S. Regan, and S. Glenzer, “Temperature measurement through detailed balance in x-ray thomson scattering,” *High Energy Density Phys.* **5**, 182 (2009).

⁷⁹S. Ferri, O. Peyrusse, and A. Calisti, “Stark–Zeeman line-shape model for multi-electron radiators in hot dense plasmas subjected to large magnetic fields,” *Matter Radiat. Extremes* **7**, 015901 (2022).

⁸⁰R. Doron, D. Mikitchuk, C. Stollberg, G. Rosenzweig, E. Stambulchik, E. Kroupp, Y. Maron, and D. Hammer, “Determination of magnetic fields based on the Zeeman effect in regimes inaccessible by zeeman-splitting spectroscopy,” *High Energy Density Phys.* **10**, 56 (2014).

⁸¹I. B. Gornushkin, L. A. King, B. W. Smith, N. Omenetto, and J. D. Winefordner, “Line broadening mechanisms in the low pressure laser-induced plasma,” *Spectrochim. Acta Part B* **54**, 1207 (1999).

⁸²G. Pérez-Callejo, T. Gawne, T. R. Preston, P. Hollebon, O. S. Humphries, H.-K. Chung, G. L. Dakovski, J. Krzywinski, M. P. Minitti, T. Burian, J. Chalupský, V. Hájková, L. Juha, V. Vozda, U. Zastra, S. M. Vinko, S. J. Rose, and J. S. Wark, “Dielectronic satellite emission from a solid-density Mg plasma: Relationship to models of ionization potential depression,” *Phys. Rev. E* **109**, 045204 (2024).

10 April 2025 18:02:44